Weierstraß-Institut
für Angewandte Analysis und Stochastik

Leibniz-Institut im Forschungsverbund Berlin e. V.

Preprint ISSN 2198-5855

Modeling, simulation, and optimization of geothermal energy production from hot sedimentary aquifers

Laura Blank[1], Ernesto Meneses Rioseco[2], Ulrich Wilbrandt[1], Alfonso Caiazzo[1]

submitted: December 11, 2019

[1] Weierstrass Institute
Mohrenstr. 39
10117 Berlin, Germany
E-Mail: laura.blank@wias-berlin.de
alfonso.caiazzo@wias-berlin.de
ulrich.wilbrandt@wias-berlin.de

[2] Leibniz Institute for Applied Geophysics
Stilleweg 2
30655 Hannover, Germany
E-Mail: Ernesto.MenesesRioseco@leibniz-liag.de

No. 2656
Berlin 2019

2010 *Mathematics Subject Classification.* 65M60, 76S05, 86-08, 86A20.

Key words and phrases. Porous and fractured geothermal reservoir modeling, geothermal multi-well configurations, finite element method, thermo-hydraulic coupling, optimization, open-source software.

Edited by
Weierstraß-Institut für Angewandte Analysis und Stochastik (WIAS)
Leibniz-Institut im Forschungsverbund Berlin e. V.
Mohrenstraße 39
10117 Berlin
Germany

Fax: +49 30 20372-303
E-Mail: preprint@wias-berlin.de
World Wide Web: http://www.wias-berlin.de/

Modeling, simulation, and optimization of geothermal energy production from hot sedimentary aquifers

Laura Blank, Ernesto Meneses Rioseco, Ulrich Wilbrandt, Alfonso Caiazzo

Abstract

Geothermal district heating development has been gaining momentum in Europe with numerous deep geothermal installations and projects currently under development. With the increasing density of geothermal wells, questions related to the optimal and sustainable reservoir exploitation become more and more important. A quantitative understanding of the complex thermo-hydraulic interaction between tightly deployed geothermal wells in heterogeneous temperature and permeability fields is key for a maximum sustainable use of geothermal resources. Motivated by the geological settings of the Upper Jurassic aquifer in the Greater Munich region, we develop a computational model based on finite element analysis and gradient-free optimization to simulate groundwater flow and heat transport in hot sedimentary aquifers, and investigate numerically the optimal positioning and spacing of multi-well systems. Based on our numerical simulations, net energy production from deep geothermal reservoirs in sedimentary basins by smart geothermal multi-well arrangements provides significant amounts of energy to meet heat demand in highly urbanized regions. Our results show that taking into account heterogeneous permeability structures and variable reservoir temperature may drastically affect the results in the optimal configuration. We demonstrate that the proposed numerical framework is able to efficiently handle generic geometrical and geologocal configurations, and can be thus flexibly used in the context of multi-variable optimization problems. Hence, this numerical framework can be used to assess the extractable geothermal energy from heterogeneous deep geothermal reservoirs by the optimized deployment of smart multi-well systems.

1 Introduction

Stored heat in the subsurface in a variety of geological settings is recognized as geothermal energy and constitutes a renewable resource that can be sustainably and environmentally-friendly recovered by diverse utilization concepts, [69, 78].

Among the many possible geothermal energy uses, geothermal district heating development has been gaining momentum in Europe with a significant installed capacity and numerous projects currently under development, [9, 10, 13, 58, 72, 102]. In particular, the Greater Munich region in Germany shows one of the most dynamic developments, [3, 5, 37, 104], where numerous deep geothermal facilities have gone into operation in the last two decades, meeting the heat demand of several villages and neighborhoods of Munich (see also Figure 1).

Research projects such as GRAME [24, 56] and GEOmaRE[1] are prominent examples of efforts taken to facilitate the German energy transition by substantially contributing to the decarbonisation of district heating networks in large cities. They clearly evidence that considerable heat demand together with significant accessible geothermal resources and an economic, technological and political commitment to the transition to renewal energy are key ingredients for a sustainable and decarbonized district heating development. Large companies such as the municipal energy supplier of Munich (Stadtwerke München - SWM) as well as large financial institutions substantially contributed to this development. According to the SWM district heating vision, the heat demand of the city of Munich should be met

[1] See https://www.enargus.de/pub/ bscw.cgi/

DOI 10.20347/WIAS.PREPRINT.2656 Berlin 2019

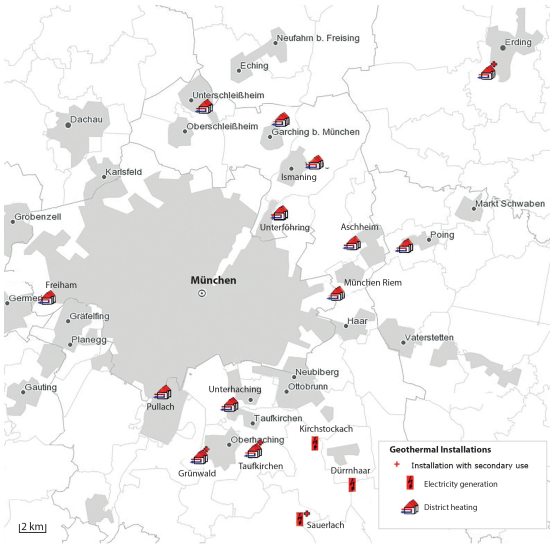

Figure 1: Geothermal facilities that have been under operation for several years in the Greater Munich region. Note that both electricity and heat are being produced. Each geothermal plant consists of a doublet or a triplet. In the case of the Unterföhring geothermal plant, two doublets are implemented. This picture has been obtained from the German geothermal information system GeotIS (`http://www.geotis.de`, June 2019, [3, 5, 8]) and has been subsequently modified.

by 2040 completely by renewable energy, [24, 56]. To accomplish this, $400\,\mathrm{MW_{th}}$ should be provided by geothermal district heating, which means that deep geothermal energy shall contribute the most to the heat transition. Therefore, numerous geothermal extraction and production wells are planned by 2040 in the city of Munich[2].

These developments show the widespread availability of low-enthalpy geothermal resources and their huge potential for district heating in densely populated urban regions. At the same time, with the increasing density of geothermal wells during the life cycle of a geothermal field development, questions related to the optimal and sustainable reservoir exploitation become more and more important, [37, 76, 77, 102, 106, 108].

For sustainability, the future deployment of wells has to be chosen in such a way that negative interference with existing neighboring wells is avoided while their positive interference is promoted. In addition, the placement and spacing of new geothermal wells and their operational schemes have to be carefully selected depending on the geometric dimensions of geothermal concession fields to avoid thermo-hydraulic encroachment. This refers specifically to the spatio-temporal evolution of the cooling front emanating from the injection wells, which is mainly controlled by the permeability structure, thickness of the aquifer, exploitation scheme (injection and production rates), and a possible thermo-hydraulic interaction with wells in the vicinity.

In the last decades, the usage of optimization algorithms to optimize well patterns has gained increasing popularity for a sustainable reservoir management in the hydrocarbon industry (see, e.g., [36, 70, 85, 94]). In contrast to geothermal exploitation concepts, the geometric well configurations normally considered in the oil and gas industry are intended to optimize the oil and gas recovery from hydrocarbon-bearing formations by efficiently sweeping the hydrocarbons towards the production wells

[2] Other outstanding examples of geothermal energy production from deep sedimentary aquifers for district heating in Europe include the numerous geothermal plants in the Paris Basin (see, e.g., [21]) and in the West Netherlands Basin (e.g., [23, 87]).

through fluid injection. In the geothermal context, however, other aspects drive the use of optimized multi-well configurations. In particular, in highly populated urban cities with a lack of space for numerous geothermal drilling sites and a huge heat demand, specific arrangements of multiple geothermal wells are of great interest. In addition to the search of an optimal geothermal site depending on the site-specific geothermal and hydrogeological conditions, the optimized multi-well configuration, spacing, and operational schemes for the economic utilization time span are among the key questions, which have not been extensively investigated yet.

The management of geothermal reservoirs aims at going through a series of decisions to achieve a sustainable and optimal exploitation of the geothermal resources. Concerning the economic lifetime of a geothermal plant based on open loops, special attention is paid to the thermal breakthrough and possible thermal short circuits, [19, 20, 68, 83, 84, 98].

Finding the optimal set of decisions among different options usually relates to maximizing an economic outcome, which in turn involves maximizing the net extraction of geothermal energy. The optimal field development and production management is thus an arduous and multi-variable optimization task with numerous parameters influencing the optimization process. Important factors include the number and type of wells, well locations, production and injection constraints, and economic factors like operating costs. The optimization task is even more challenging due to geological uncertainties associated with reservoir petrophysical parameters (e.g., thermal conductivity, porosity, and permeability) varying over a wide range of values and heterogeneities of subsurface domains (e.g., temperature, pressure, and permeability fields).

As reliable and quantitative tools, mathematical modeling and computer simulation of geothermal reservoir processes, especially in connection with optimization problems related to multi-well configurations and well patterns, have received considerable attention in the last years. Several recent works employ diverse numerical methods (e.g., finite difference, finite volume, or finite element) as well as different approaches to solve related optimization problems. Among others, [37] proposed a thermo-hydraulic model of the geothermal Upper Jurassic aquifer in the Munich region, based on a finite element method, in order to forecast long-term temperature and pressure fields in multi-well configurations. Based on this model, preliminary aspects of the optimal design problem were recently investigated and presented in [76, 77], numerically confirming advantages of doublet arrays compared to a single doublet. The modeling of hot sedimentary aquifers was also investigated in [108] and [32], taking into account the impact of sandstone reservoir heterogeneities on geothermal doublets production performance.

Reservoir lifetimes for doublets in hot sedimentary aquifers were recently studied in [92, 93], and in [106], including lattice-type configurations and sizes of geothermal concession fields. Very recently, automatic optimization methods based on genetic algorithms have been proposed in [90, 109], considering heterogeneous reservoirs but limited to Cartesian meshes. Further, in [62] a gridblock-based optimization strategy with a stochastic optimization is tested.

Great efforts have been made also in the development of software frameworks for the simulation of groundwater flow and heat and mass transport in porous and fractured geologic media. Among the most popular tools, there are several commercial packages as FEFLOW developed by DHI-WASY GmbH, COMSOL Multiphysics developed by COMSOL, MOOSE developed by the Idaho National Laboratory, TOUGH2/TOUGHREACT developed by the Earth Science Division of the Lawrence Berkeley National Laboratory, and FLUENT developed by ANSYS Inc., to mention a few.

Commercial software can be used by practitioners without requiring particular knowledge about the details of the numerical discretizations. However, this aspect makes it relatively difficult to further develop these packages for user-specific purposes and/or to tackle new research questions. The multi-physical

nature of geothermal reservoirs requires collaborative and interdisciplinary research, combining the most recent advantages in mathematical modeling, simulation, computational geometry and, as in the case of this paper, optimization. This is one of the reasons that motivated, especially in latest years, the initiation of several open-source projects for collaborative software platforms. In the context of groundwater flow modeling, notable projects include Open Porous Media[3], OpenGeoSys[4], DuMuX[5], and MODFLOW [75] besides other packages developed for a broader range of applications, such as FEniCS [7], DUNE [18] or deal.II [11]. The interested reader is referred to [15] for an extensive review of open source packages as well as for a detailed discussion on the benefit of open source platforms.

We present a numerical model based on the finite element approximation of a general Darcy–Brinkman problem, suitable for a wide range of physical parameters, including larger permeabilities, coupled to a finite element solver for the temperature field. The model is based on the mixed (or dual) formulation of the groundwater flow problem. Unlike the simpler (and widely used in the context of geothermal modeling, e.g., [35]) primal formulation, in which the numerical solution is computed only for the pressure, in the mixed form the problem is solved for both velocity and pressure. At the expense of a slightly higher computational complexity, the mixed form allows to compute more regular velocity fields. Moreover, we use the mixed formulation in combination with a non-matching (immersed) method to account for the boundary conditions at the wells as *singular* forces. An analogous approach has been also used in several previous works (e.g., [35, 106]), but only for the primal formulation and restricted to the case of point-associated wells located at mesh vertices. In this paper, we show that based on the mixed Darcy–Brinkman problem, the imposition of singular sources/sinks of mass can be decoupled from the spatial discretization. From the practical viewpoint, this is a major advantage especially when the simulation of numerous scenarios of multiple well arrangements is intended, as it does not require the regeneration of the computational mesh.

In the context of sustainable and optimized geothermal energy production by selected smart multi-well patterns, the scope of this work is to present a fit-for-purpose computational model of coupled groundwater flow and heat transport, integrating an optimization algorithm with diverse geothermal multi-well arrangements. The numerical framework includes the development of a mathematical model that enables a quantitative assessment of maximum sustainable production of geothermal energy, taking into account the underground temperature field, thermal and hydraulic property distributions, as well as thermo-hydraulic interactions between neighboring wells. Heat transport mainly by advective and diffusive processes in porous, fractured, and karstified reservoirs in the framework of the equivalent porous medium (EPM) approach is computed in this work (see, e.g., [50]). Although we focus on similar reservoir conditions as found in the Upper Jurassic carbonates in the Munich region, the methodology developed here can be applied to any hot sedimentary aquifer.

Regarding the optimization of geothermal energy extraction, the main goal of this work is to describe and quantify the thermo-hydraulic effects on the placement and spacing of different geothermal multi-well patterns with varying geothermal and hydrogeological conditions. Therefore, we concentrate on parameters that specify the arrangement of the wells. However, the approach can be extended to an arbitrary number of control variables (e.g., injection and production flow rates, injection temperatures, etc.). These problems as well as the use of more efficient optimization methods are subjects of ongoing research. One of the important capabilities of the optimization method used in this work is to search in narrow and tight spaces through the entire geothermal reservoir to select optimal placements of multi-well configurations and spacing parameters. This relates to maximizing the net energy production during the life-cycle of geothermal reservoir development. Advantages and disadvantages

[3] https://opm-project.org/
[4] https://opengeosys.org
[5] https://dumux.org

of the utilization of different multi-well configurations are discussed.

We restrict in this work to a fit-for-purpose numerical modeling of geothermal reservoirs in two dimensions, studying diverse scenarios of multiple geothermal well arrangements in varying geothermal and hydrogeological conditions in a reasonable time frame.

A further motivation of our work is the assessment of open-source tools to tackle the optimization problem. The above described numerical method has been implemented in the open source finite element library ParMooN, developed at the WIAS, [105]. The optimization problem is solved with a gradient-free, global optimization algorithm, which has been implemented within the open source library NLopt. In particular, we perform a detailed validation of the numerical schemes against reference and analytical solutions, investigating the sensitivity with respect to the discretization parameters (spatial and temporal mesh sizes) and the boundary conditions.

The rest of the paper is organized as follows. Section 2 aims at introducing the geothermal and hydrogeological settings that are employed to determine the details of the simulations. In Section 3 the main ingredients of our computational framework are presented: the groundwater flow model, the heat transport model, the optimization algorithm, and the corresponding numerical schemes. In Section 8 we describe the different scenarios which are investigated computationally, while Section 9 is dedicated to the results of our numerical simulations. Conclusions are drawn in Section 10.

2 Geothermal and hydrogeological setting

The thermo-hydraulics of geothermal reservoirs is based on the combination of a geothermal and a hydrogeological model. Therefore, considerable effort should be taken to characterize both the geothermal and hydrogeological conditions normally encountered in hot sedimentary aquifers.

Detailed knowledge on underground temperature distribution is crucially important for the assessment of geothermal energy potential. The temperature field in hot sedimentary aquifers mainly found in intracratonic basin or orogenic belt/foreland basin geothermal play types is predominantly driven by natural heat conduction, [53, 78, 91]. A near average heat flow is recognized as the heat source in deep seated aquifers in conduction-dominated hydrothermal systems, [12, 40, 42, 55, 78, 99].

Roughly, an average geothermal gradient of around $30\,^{\circ}\mathrm{C}$ per kilometer is established in these geothermal play types. Ample data on temperature measurements has been gathered by the hydrocarbon industry through oil and gas exploration in sedimentary basins, and subsequently corrected and put into a geothermal context [3–5]. Moreover, geothermal exploration has contributed to the understanding of subsurface temperature distribution in sedimentary basins, [41, 65, 96]. In addition, thermal properties of different reservoir rocks, i.e., thermal conductivity, volumetric heat capacity, and thermal diffusivity, have been measured and described in, e.g., [28, 30, 31, 45, 46, 63, 67, 97].

Since the South German Molasse Basin and in particular the Bavarian Molasse Basin is one of the best studied foreland basins and the only geothermally developed foreland basin worldwide, [37, 38, 59, 78, 79], extensive geoscientific data has been collected. Especially, the porous, fractured, and karstified Upper Jurassic carbonates of the South German Molasse Basin are recognized as the most important hydrothermal reservoir for deep geothermal energy utilization in Germany and Middle Europe, [37, 38, 51, 52, 54, 57, 73].

Due to this remarkable development and the related increasing concentration of geothermal wells, we focus in this work on similar geothermal and hydrogeological conditions as encountered in the Upper Jurassic (Malm) aquifer in the Greater Munich region. However, as mentioned earlier, the methodol-

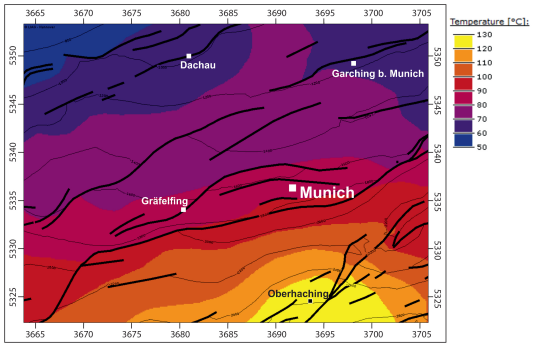

Figure 2: Temperature distribution at the top Upper Jurassic (Malm) formation in the Bavarian Molasse Basin. Note the temperature range in southern urban Munich between 80 and $100\,^{\circ}\mathrm{C}$. Black thick lines display major faults that cross the Malm aquifer. This picture is based on the compiled database at the LIAG and stems from GeotIS [3, 8]. It has been modified.

ogy developed in this work can be applied to other low-enthalpy geothermal reservoirs that classify as hot sedimentary aquifers. Figure 2 displays the temperature distribution at the top Upper Jurassic formation in the Greater Munich region. Due to the down-bending of the lithosphere from North to Southeast towards the Alpine Orogenic Belt, a laterally and vertically varying temperature field reigns in the Upper Jurassic aquifer (see Figures 2 and 3). Based on this fact, some of the scenarios considered for the well placement optimization in this work include the effect of a laterally varying temperature field. Furthermore, a present-day average surface heat flow of around $65\,{}^{\mathrm{mW}}/_{\mathrm{m}^2}$ and an average surface temperature of approximately $10\,^{\circ}\mathrm{C}$ have been documented in the literature for Germany, [4, 25, 58, 74, 80]. In particular, in the Bavarian Molasse Basin the surface heat flow varies between 60 and $80\,{}^{\mathrm{mW}}/_{\mathrm{m}^2}$, [44].

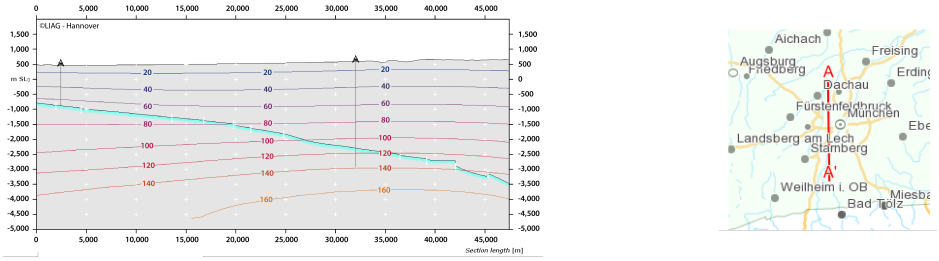

Figure 3: Vertical profile (top picture) of the temperature distribution along a North-South oriented line that crosses the city of Munich (from left to right corresponds to the profile from A to A' in the bottom picture). The Upper Jurassic formation is depicted in blue greenish color. Note the threefold vertical exaggeration and the southwards declination of the Upper Jurassic formation (towards the Alps). This picture has been built with GeotIS [3, 8]).

When it comes to the hydraulics of groundwater in hot sedimentary aquifers, one-phase, liquid-dominated, laminar fluid dynamics is normally considered in confined and saturated reservoir conditions. Besides, fluid flow in clastic and carbonate reservoirs occurs in many different aquifer types such as porous, fractured, and karstified aquifers, [1, 2]. Geologically modeling the heterogeneities and anisotropies encountered in such aquifers remains an ongoing effort, [26].

Since permeability is the main control on fluid flow and consequently on heat and mass transport in aquifers, the characterization of the permeability structure of hot sedimentary aquifers is a key ingredient for a sound assessment of geothermal reservoir performance. Concerning reservoir quality of deep

sandstone and carbonate aquifers encountered in foreland basin and intracratonic basin geothermal play types in Europe, ample data in terms of porosity and permeability parameter ranges has been published (e.g., [14, 34, 64, 66, 81]). In particular, a large set of hydraulic conductivity and permeability values has been published in [37, 100, 101].

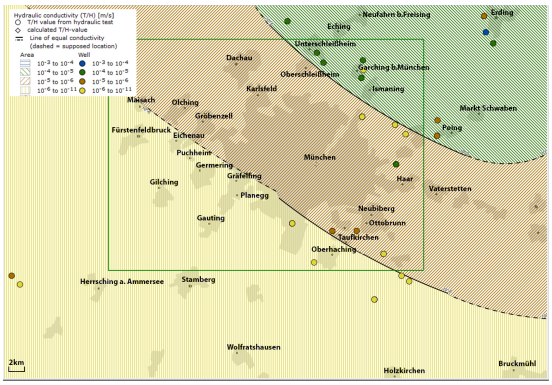

Figure 4: Regional hydraulic conductivity trend for the Upper Jurassic formation in the Greater Munich region. Shaded areas show urban regions. The green rectangle displays the area represented in Figure 2. Note the regional trend of decreasing hydraulic conductivity in the southwestern direction. This picture is based on the compiled database at the LIAG and results from the work done by [16]. It originates from GeotIS [3, 8] and has been modified.

The regional and local natural groundwater flow in hot sedimentary aquifers is mainly dominated by the existing hydraulic gradient and the permeability structure of the aquifer at hand. It is in general overprinted by the relatively high flow rates, imposed by the permanent production and injection rates used for heat extraction in numerous multi-well arrangements, [59]. In the case of the Upper Jurassic aquifer in the South German Molasse Basin, numerous pump and injection tests have been analyzed in, e.g., [16, 100]. Particularly concerning the hydraulic activity of fault damage zones, it is still debated for the case of the Upper Jurassic aquifer in the Bavarian Molasse Basin whether linear (controlled by the fault damage zone permeability), radial (controlled by the matrix permeability), or bilinear (combined linear flow in perpendicular directions in both the fault and the matrix) is the dominant flow regime, [16, 82]. However, most of the related, published studies claim that the majority of the hydraulically tested fault damage zones of the Upper Jurassic aquifer in the Greater Munich region shows a rather radial flow regime, [16]. Fundamentally, the ratio between matrix and fault damage zone permeability controls what kind of flow regime predominates, whether linear, radial, or bilinear flow.

Recently, a multidisciplinary geothermal reservoir characterization of the Upper Jurassic aquifer (Malm) in the Greater Munich region has been conducted in [37]. The combination of a variety of geophysical and geological data led to reliable hydraulic reservoir properties and sound knowledge of the permeability structure. Regional and local structural-geological elements as well as facies distribution were integrated in a geothermal reservoir model. Carbonate reservoirs are distinguished by their highly variable permeability structure. The work of [37] presents a wide range of hydraulic conductivity values in the order of 10^{-4} to $10^{-9}\,\mathrm{m/s}$. The incorporation of outcrop data, main inflow zones data in geothermal boreholes, multiple logging data of several geothermal and hydrocarbon wells in the region, and pump and injection test data led to a simplified hydrostratigraphic standard profile of the Upper Jurassic aquifer in the Munich region, presented in [37]. Based on these reservoir characterization and modeling results, some scenarios with laterally varying hydraulic conductivity (or the respective permeability), which is caused by the presence of different carbonate facies or by fault damage zones, are considered in the present work in order to assess its effect on the well placement optimization. Figure 4 shows the overall hydraulic conductivity of the Upper Jurassic geothermal reservoir, which decreases

from North to Southwest as the Malm aquifer deepens towards the Alpine orogenic front (see also Figure 3). Besides, the overriding cretaceuos and tertiary layers and the underlying crystalline basement, which delimit the Malm aquifer, are considered as hydraulically non-conductive (aquitards). Based on existing drinking water wells and thermal water boreholes, an equipotential line map for the thermal water in the Malm of the Southern German Molasse Basin was built by [43] but the currently ongoing discussion suggests a revision of the normalization procedure in the identification of groundwater potential. Due to the still large uncertainties with regard to the current groundwater flow regime in the Malm aquifer and the existing, comparatively low hydraulic gradient, a constant underlying pressure field can alternatively be considered for the thermo-hydraulic modeling.

3 Mathematical model

The mathematical model developed in this work consists of two components: Firstly, a fluid flow model for a confined and saturated aquifer, which is assumed to be predominantly composed of consolidated sedimentary material as, e.g., sandstone and/or carbonates. Secondly, an advection-diffusion model for the temperature distribution.

These two problems are sequentially coupled, i.e., the velocity solution of the Darcy–Brinkman problem determines the advective field used in the differential equation describing the temperature evolution.

Based on the geothermal and hydrogeological setting described in Section 2, the model is build upon the following assumptions:

(A1) We consider an aquifer confined by overriding and underlying aquitards. As a consequence, fluid flow through the top and bottom boundaries of the reservoir is neglected. Moreover, assuming that the vertical dimension is much smaller than the horizontal characteristic size, we neglect the effect of gravitational forces (two-dimensional approximation).

(A2) Groundwater flow is modeled by the Brinkman equations, [22]. Compared to the frequently used Darcy model, an additional term accounting for viscous stresses is present in the momentum balance equation. This allows to go beyond the range of validity of Darcy's law towards regimes of higher permeability, which is particularly interesting for vuggy porous media resulting from, e.g., karstification and highly damaged zones in faulted domains (see, e.g., [61, 88]).

(A3) Steady-state flow of a single-phase, incompressible, Newtonian fluid in an isotropic, saturated, non-deformable aquifer, taking into account the equivalent porous medium approach for possibly karstified and fractured domains that exhibit high permeabilities.

(A4) The dependence of fluid viscosity and fluid density on temperature is neglected for the range of temperatures considered.

(A5) The heat transport model is confined to the aquifer under investigation, i.e., heating or cooling due to the temperature of the aquitards is neglected.

(A6) The thermal dispersion is in most cases dominated by the longitudinal contribution, such that the transversal dispersion is neglected in the following. Further, we consider a temperature-independent volumetric heat capacity and thermal conductivity.

3.1 Aquifer model

The domain of interest is an aquifer of constant thickness $H\,[\mathrm{m}]$ with rectangular base of diameter $L\,[\mathrm{m}]$, with $H \ll L$. Each well is modeled as a cylindrical borehole $w_{3D}^{(\star)}$, see Figure 5.

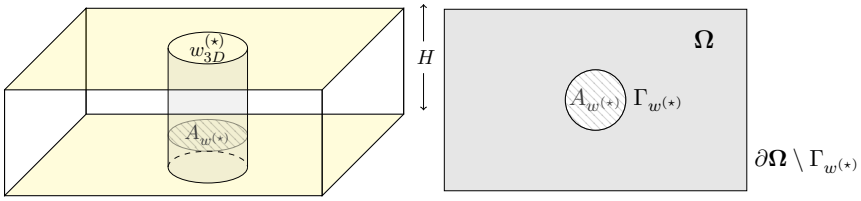

Figure 5: Left: Schematic 3D model of an aquifer, fully penetrated by a single cylindrical well $w_{3D}^{(\star)}$. Top and bottom of the aquifer (yellow) are impermeable for fluid. Right: A horizontal cross-section.

In the horizontal direction, the fluid is allowed to permeate through the medium boundaries, while eventual phenomena in the vertical direction are neglected. Hence, for the remainder of this work we focus on a 2D slice, parallel to the confining planes, as illustrated in Figure 5 (right). Let $\mathbf{\Omega} \subset \mathbb{R}^2$ be the spatial domain under consideration. We denote by $w^{(\star)}$ the 2D slice of the well with cross-sectional area $A_{w^{(\star)}}\,[\mathrm{m}^2]$ and by $\Gamma_{w^{(\star)}}$ the boundary of $w^{(\star)}$.

Later on we will distinguish between production wells and injection wells by using the respective symbol $(\star) \in \{\mathrm{prod}, \mathrm{inj}\}$. The same notation is adopted for other quantities that are associated to production and injection wells, respectively.

3.2 Groundwater flow

3.2.1 The Darcy–Brinkman model

Assuming conservation of mass and (linear) momentum, we model fluid flow via the stationary Brinkman (or Darcy–Brinkman) equations, [22]:

$$-\mu_{\mathrm{eff}}\,\Delta \boldsymbol{u} + \nabla p + \sigma \boldsymbol{u} = \mathbf{f} \qquad \text{in } \mathbf{\Omega}, \tag{1a}$$

$$\nabla \cdot \boldsymbol{u} = g \qquad \text{in } \mathbf{\Omega}, \tag{1b}$$

where $\boldsymbol{u} : \mathbf{\Omega} \to \mathbb{R}^2\,[\mathrm{m/s}]$ is the velocity field, $p : \mathbf{\Omega} \to \mathbb{R}$ [Pa] is the pressure field, $\mu_{\mathrm{eff}}\,[\mathrm{kg/(m\,s)}]$ denotes the effective viscosity, and $\sigma := \mu K^{-1}$, i.e., the fraction of fluid viscosity $\mu\,[\mathrm{kg/(m\,s)}]$ and permeability $K\,[\mathrm{m}^2]$ of the porous medium. Moreover, $\boldsymbol{f}\,[\mathrm{N/m^3}]$ models external volume forces, while $g\,[\mathrm{s}^{-1}]$ takes into account sources or sinks of mass. For the considered two-dimensional case, external volume forces as well as mass sources within the aquifer vanish in (1a)-(1b).

Problem (1) is completed by with the following boundary conditions. Along each well boundary, a constant velocity magnitude $U_{w^{(\star)}}\,[\mathrm{m/s}]$ directed normally to the well boundary is assumed, yielding the Dirichlet boundary conditions

$$\boldsymbol{u} = \pm U_{w^{(\star)}} \boldsymbol{n}_{w^{(\star)}} \qquad \text{on } \Gamma_{w^{(\star)}},\ \forall w^{(\star)}, \tag{1c}$$

where $\boldsymbol{n}_{w^{(\star)}}$ is pointing from the well into the porous medium (inner unit normal vector). Positive and negative signs in front of $U_{w^{(\star)}}$ shall be used to represent flow into (injection) or out of (production)

the aquifer with respect to the well, respectively. The value of the in-/outflow velocity, $U_{w^{(\star)}}$ in (1c), depends on the prescribed injection and production rate, respectively, and the thickness $H\,[\mathrm{m}]$ of the aquifer (see Subsection (3.1)). Let us assume that the fluid is injected or extracted uniformly along the vertical direction of the generic cylindrical well ${w_{3D}}^{(\star)}$ with flow rate $Q^{(\star)}_{w_{3D}}\,[\mathrm{m}^3/\mathrm{s}]$. Then the magnitude of the velocity along the well boundary for the two-dimensional problem is given by

$$U_{w^{(\star)}} = \frac{Q^{(\star)}_{w_{3D}}}{2\pi r_{w^{(\star)}} H} \quad \text{ on } \Gamma_{w^{(\star)}}, \tag{2}$$

with $r_{w^{(\star)}}\,[\mathrm{m}]$ denoting the radius of the well.

Neumann boundary conditions are imposed on the outer boundary, setting the external pressure equal to a given function, i.e.,

$$(\mu_{\mathrm{eff}}\,\nabla \boldsymbol{u} - p\mathbb{I}) \cdot \boldsymbol{n} = P\boldsymbol{n} \qquad \text{on } \partial\boldsymbol{\Omega} \setminus \textstyle\bigcup_{w^{(\star)}} \Gamma_{w^{(\star)}}, \tag{3}$$

where $\boldsymbol{n}$ stands for the outer unit normal vector.

A constant pressure (set to $P = 0$ Pa) at the aquifer boundaries is used in the computations described in Section 9, assuming that natural flow in the geothermal reservoir can be neglected in comparison to the flow induced by operating injection and production wells (see Section 2).

Remark 4 (Darcy versus Brinkman formulation)
If inertia forces are small compared to damping/resistive forces, the system (1a)-(1b) *naturally reduces to the classical Darcy model. In case the targeted reservoir region contains hydraulically conductive fractures, fault damage zones, or karstified domains, high permeabilities might lead to groundwater flow regimes, where the interaction of fluid particles (inertial forces) becomes relevant, making the use of the more general Brinkman model* (1) *necessary. As explained in further detail in Section 4.2, the numerical method designed and employed to approximately solve equation* (1) *is robust with respect to the physical parameters (μ_{eff} and σ), i.e., it can be used in a similar manner for the Darcy limit as well.*

4.0.2 Model of wells through singular forces

In deep geothermal applications, the radii of the cylindrical wells, e.g., $0.1\,\mathrm{m}$ in [107], are much smaller than the scale of the domain (several kilometers). The presence of this wide range of spatial scales might considerably increase the computational complexity if the computational mesh is required to accurately resolve the well boundary. In order to circumvent this issue, we employ the so-called *immersed boundary method* [86], which is based on considering an extended domain, which includes the well regions and describes the limit case when the well radii tend to zero. The wells are then described as singular forces defined in single points (the well centers).

Accordingly, we consider a flow problem defined over an extended domain $\widehat{\boldsymbol{\Omega}} := \boldsymbol{\Omega} \cup \left(\bigcup_{w^{(\star)}} w^{(\star)}\right)$ (see Figure 5 bottom), where the presence of wells is taken into account assuming that the divergence of the velocity field vanishes everywhere except for the centers of injection and production wells. This is modeled via singular sources (or sinks) of mass in equation (1b), i.e.,

$$\nabla \cdot \boldsymbol{u} = \sum_{l=1}^{N^{\mathrm{inj}}+N^{\mathrm{prod}}} g_{w_l^{(\star)}} \delta_{w_l^{(\star)}} \quad \text{ in } \widehat{\boldsymbol{\Omega}}. \tag{4}$$

Here, N^{inj} is the number of injection wells, N^{prod} refers to the number of production wells, $\delta_{w_l^{(\star)}}$ denotes the Dirac delta distribution with respect to the well center, and $g_{w_l^{(\star)}}$ are proper constants which depend on the prescribed injection respectively production rates.

Let us consider the case of a single well $w^{(\star)}$. In order to determine the singular force $g_{w^{(\star)}}$, we note that the solution of the problem with the original boundary condition (1c) satisfies

$$\int_{w^{(\star)}} \nabla \cdot \boldsymbol{u} = \int_{\Gamma_{w^{(\star)}}} \boldsymbol{u} \cdot \boldsymbol{n}_{w^{(\star)}} = \pm U_{w^{(\star)}} 2\pi r_{w^{(\star)}} = \pm \frac{Q_{w_{3D}}^{(\star)}}{H}, \tag{5}$$

where we have used the Gaussian theorem, the boundary condition (1c), the fact that

$$|\Gamma_{w^{(\star)}}| = 2\pi r_{w^{(\star)}},$$

and the expression (2) for $U_{w^{(\star)}}$. On the other hand, integrating (4) over the boundary of the circle $w^{(\star)}$, using (5), the fact that $g_{w^{(\star)}}$ is constant, and the property $\int_{w^{(\star)}} \delta_{w^{(\star)}} = 1$ of the Dirac delta distribution, we obtain

$$g_{w^{(\star)}} = \int_{w^{(\star)}} g_{w^{(\star)}} \delta_{w^{(\star)}} = \int_{w^{(\star)}} \nabla \cdot \boldsymbol{u} = \pm \frac{Q_{w_{3D}}^{(\star)}}{H}\,. \tag{6}$$

Hence, we replace the flow problem (1) with a problem defined on $\widehat{\boldsymbol{\Omega}}$. Instead of the Dirichlet boundary condition (1c), the prescribed flow rate is then imposed via the modified mass conservation equation (4).

One of the main advantages from the practical point of view is that the immersed method allows for a coarser spatial discretization, thus reducing the computational effort for the numerical simulation. Immersed methods have been previously used in the context of simulation of perfusion within biological tissues [27, 33] as well as in [35] for the simulation of groundwater flow. In this latter case, however, the singular problem was derived from the primal Darcy formulation, instead of the mixed general Darcy–Brinkman problem.

At the discrete level, there are different approaches to include the singular forces in (4) in a numerical method. One possibility is to assume that the points, where the singular sources and sinks are defined, coincide with vertices (or edges in 3D) of the considered computational mesh (see, e.g., [33,35]). This choice, however, strongly links the singular sources to the mesh generation.

We adopt a *non-matching* approach, decoupling the singular points from the the spatial discretization. To this purpose, we approximate the right-hand side of (4) with a discrete version of the Dirac delta distribution, with support on a small neighborhood of the well center.

We consider a classical approximation δ^{r_ε} (see also [86])

$$\delta_{w^{(\star)}}^{r_\varepsilon}(x,y) := \frac{\pi}{r_\varepsilon^2\,(\pi^2-4)}\theta\left(\frac{d_{w^{(\star)}}(x,y)}{r_\varepsilon}\right), \tag{7}$$

where

$$d_{w^{(\star)}}(x,y) = \sqrt{(x-x_{w^{(\star)}})^2 + (y-y_{w^{(\star)}})^2}$$

denotes the distance from the center $(x_{w^{(\star)}}, y_{w^{(\star)}})$ of the well $w^{(\star)}$ and

$$\theta(r) := \begin{cases} \cos(\pi r) + 1, & \text{if } -1 < r < 1, \\ 0, & \text{otherwise.} \end{cases} \tag{8}$$

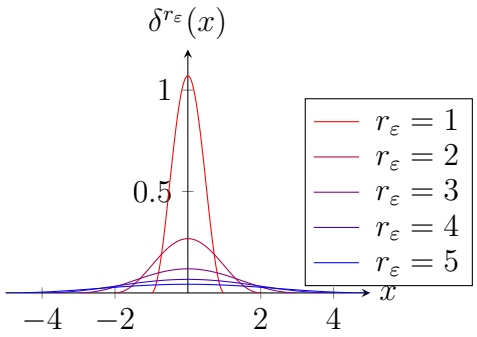

Figure 6: Visualization of (7) for $y = y_{w^{(\star)}}$ and $x_{w^{(\star)}} = 0$. The function vanishes for the points at distance from $(x_{w^{(\star)}}, y_{w^{(\star)}})$ greater than r_ε. Notice that, for any $r_\varepsilon > 0$, the integral over $\widehat{\mathbf{\Omega}}$ of the function $\delta^{r_\varepsilon}_{w^{(\star)}}$ is equal to one.

In (7), $r_\varepsilon > 0$ is an arbitrary (small, compared to the domain size, i.e., $r_\varepsilon \ll \operatorname{diam}(\widehat{\mathbf{\Omega}})$) parameter that can be chosen depending on the well radius and on the suitable spatial discretization (near the well). For a visualization of δ^{r_ε} for different values of r_ε, see Figure 6.

In practice, the singular term is defined in such a way that the physical solution, prescribed only outside the well, is continuously extended inside the well. As a consequence, the numerical solution will have a physical meaning only at a distance from the well center greater than or equal to r_ε.

One of the main advantages of the non-matching approach is that it allows to arbitrarily change the position of the well within the computational domain without the need of re-generating the computational mesh. This feature will be extremely important when solving the optimization problem related to the (arbitrary) optimal placement of the wells.

4.1 Heat transport

4.1.1 The advection-diffusion equation

The model for heat transport can be obtained from the standard energy conservation equation (see, e.g., [93]), resulting in a time-dependent advection-diffusion equation for a temperature field $T\,(t, \boldsymbol{x})$ $[\mathrm{K}]$:

$$\frac{\partial\,(\rho\, C T)}{\partial t} - \nabla \cdot (\lambda \nabla T) + \rho_f C_f\, \boldsymbol{u} \cdot \nabla T = 0 \qquad \text{in } (0, t^L] \times \mathbf{\Omega}, \tag{9a}$$

where it is assumed that heat creation through friction in the well and heat loss/gain from the outside can be neglected, yielding a right-hand side equal to zero. We complete (9a) with the initial condition

$$T(0, \boldsymbol{x}) = T_0\,(\boldsymbol{x}) \qquad \text{in } \mathbf{\Omega}, \tag{9b}$$

and the boundary conditions

$$T = T_{w_k^{\mathrm{inj}}} \qquad \text{on } \Gamma_{w_k^{\mathrm{inj}}},\ \forall k, \tag{9c}$$

$$T = T_0 \qquad \text{on } \partial\mathbf{\Omega} \setminus \bigcup_k \Gamma_{w_k^{\mathrm{inj}}}. \tag{9d}$$

Here, $k = 1, \dots, N^{\mathrm{inj}}$, N^{inj} is the number of injection wells, $T_{w_k^{\mathrm{inj}}}\,[\mathrm{K}]$ are the corresponding injection temperatures, and $T_0\,[\mathrm{K}]$ refers to the initial temperature field, in this context called *formation or aquifer temperature*. Moreover, $\boldsymbol{u}\,[\mathrm{m/s}]$ is the groundwater flow velocity, obtained from (1), $t\,[\mathrm{s}]$ is the time variable, and $t^L\,[\mathrm{s}]$ denotes the upper bound on the time interval, coinciding with the maximum operational time of the geothermal installation in the considered problems.

In (9a) there are coefficients associated to the fluid (index f) and to the porous structure (index s) respectively, namely the densities $\rho_f, \rho_s\,[\mathrm{kg/m^3}]$ and the material specific heat capacities $C_f, C_s\,[\mathrm{J/kg\,K}]$, which are combined to the volumetric (macroscopic) heat capacity, given by

$$\rho C := (1-\phi)\,\rho_s\,C_s + \phi\rho_f\,C_f,$$

depending on the porosity ϕ.

The total thermal conductivity tensor $\lambda\,[\mathrm{W/m\,K}]$ can be modeled (see, e.g., [32, 95]) as the sum of the equivalent conductivity $\lambda_{eq}\mathbb{I}$ and thermal dispersion λ_{dis}, i.e., $\lambda = \lambda_{eq}\mathbb{I} + \lambda_{dis}$ with

$$\begin{aligned} \lambda_{eq} &= (1-\phi)\,\lambda_s + \phi\lambda_f, \\ \lambda_{dis} &= \rho_f C_f \left(\alpha_T |\boldsymbol{u}| \mathbb{I} + (\alpha_L - \alpha_T) \frac{\boldsymbol{u}\boldsymbol{u}^T}{|\boldsymbol{u}|} \right) . \end{aligned} \tag{10}$$

In (10), λ_s and λ_f are the (scalar) thermal conductivities of the indexed species, $\alpha_L\,[\mathrm{m}]$ is the longitudinal thermal dispersion, and $\alpha_T\,[\mathrm{m}]$ denotes the transversal thermal dispersion.

As mentioned in (A4) and (A6), the transversal dispersion is neglected, assuming that its effect does not play a relevant role in the considered two-dimensional model and the assumption of temperature-independent densities and heat capacities further allows to exclude the respective terms from the temporal and spatial derivative.

4.1.2 Total simulation time

In our numerical simulations, the final simulation time t^L will be defined depending on two conditions. On the one hand, we consider a maximum admissible operational time of 80 years, which might depend on geological, engineering, and legal constraints. One the other hand, we consider also the so-called *specific lifetime* of the installation, which is defined as the time when the fluid temperature at a measurement point of a production well drops below a threshold temperature $T_{\mathrm{quit}}\,[\mathrm{K}]$, respectively drops by more than 10% with respect to the aquifer temperature. The specific lifetime relates to the *economic lifetime* of a geothermal facility, commonly defined as a certain limit of production temperature under which it is no longer economic to proceed.

4.1.3 Reduced-order model for the injection well

As done for the flow model (1), we consider a modified problem for the temperature field, defined on the whole domain $\widehat{\Omega}$, and in the limit case of well radius tending to zero. To this purpose, we replace the Dirichlet boundary condition at the injection wells (9c) with appropriate terms, which allow to seek for a temperature field $T\colon (0, t^L] \times \widehat{\Omega} \to \mathbb{R}$ that satisfies the condition (9c) and obeys to the equation (9a) outside the wells. The considered temperature equation is based on a penalty method, i.e., we explicitly add terms that penalize deviations from the prescribed injection temperatures within the well regions. As a consequence, an explicit spatial discretization of the well boundary is no longer

required, considerably reducing the complexity of the spatial discretization, especially in the framework of optimization.

Let us note that the temperature field is only disturbed at the injection wells such that solely these positions have to be included as heat sources. After dividing the equation (9a) by $\rho_f C_f$ we obtain

$$\begin{aligned} a\frac{\partial T}{\partial t} - \nabla \cdot (d\nabla T) + \boldsymbol{u} \cdot \nabla T \\ + \gamma \sum_{k=1}^{N^{\mathrm{inj}}} \frac{Q_{3D}^k}{H} \delta_{w_k} (T - T_{w_k}) = 0 \text{ in } (0, t^L] \times \widehat{\boldsymbol{\Omega}}, \end{aligned} \tag{11}$$

with $a := \frac{\rho C}{\rho_f C_f}$, $d := \frac{\lambda}{\rho_f C_f}$, and a dimensionless penalty parameter $\gamma > 0$. Problem (11) is then completed with the initial and boundary conditions

$$\begin{aligned} T(0, \boldsymbol{x}) &= T_0(\boldsymbol{x}) \quad \text{in } \widehat{\boldsymbol{\Omega}}, \\ T &= T_0 \qquad \text{on } \partial\widehat{\boldsymbol{\Omega}}. \end{aligned} \tag{12}$$

4.2 Numerical method

The partial differential equations for groundwater flow and heat transport are solved using a finite element method (FEM). To this purpose, let us introduce a spatial discretization (a computational mesh) $\mathcal{T}_h$ of the extended domain $\widehat{\boldsymbol{\Omega}}$, composed of shape-regular triangular elements (non-degenerate, see [29, p. 124], [39, Def. 1.107]). The parameter $h > 0$, denotes the characteristic mesh size, which can be defined, e.g., as $h := \max_{\boldsymbol{T} \in \mathcal{T}_h} h_{\boldsymbol{T}}$, where $h_{\boldsymbol{T}}$ stands for the diameter of the mesh element $\boldsymbol{T} \in \mathcal{T}_h$. Further, we will abbreviate the standard L^2-product on $A \subset \widehat{\boldsymbol{\Omega}}$ by $(\cdot, \cdot)_A$.

4.2.1 Stationary Darcy–Brinkman equation

We employ a stabilized finite element method for the Brinkman problem, which has been recently described and analyzed in [17] and is designed to deal robustly with any choice of physical parameters (i.e., μ_{eff} and σ).

The numerical approximations of the velocity and the pressure are sought in the space of continuous, piece-wise (on each triangle) linear polynomials

$$\begin{aligned} \boldsymbol{V}_h &:= \left\{ \boldsymbol{v}_h \in \boldsymbol{C}^0(\overline{\widehat{\boldsymbol{\Omega}}}) \colon \boldsymbol{v}_h|_{\boldsymbol{T}} \in \mathbb{P}_1(\boldsymbol{T}), \forall \boldsymbol{T} \in \mathcal{T}_h \right\}, \\ Q_h &:= \left\{ q_h \in L_0^2(\widehat{\boldsymbol{\Omega}}) \cap C^0(\overline{\widehat{\boldsymbol{\Omega}}}) \colon q_h|_{\boldsymbol{T}} \in \mathbb{P}_1(\boldsymbol{T}), \forall \boldsymbol{T} \in \mathcal{T}_h \right\}. \end{aligned}$$

The stabilized finite element formulation is obtained multiplying the momentum conservation equation by a function $\boldsymbol{v}_h \in \boldsymbol{V}_h$ and the mass conservation equation by $q_h \in Q_h$, and using integration by parts.

The choice of equal-order linear finite element spaces allows to reduce the computational complexity of the problem, especially when fine spatial discretizations are needed. In order to guarantee stability and convergence of the resulting numerical method, the inherent integral formulation needs to be modified, including so-called stabilization terms. We refer the interested reader to [17] (and references therein) for a detailed discussion on the stabilization methods.

The considered finite element problem for reads then:
Find $(\boldsymbol{u}_h, p_h) \in \boldsymbol{V}_h \times Q_h$ such that

$$\begin{aligned} \mu_{\text{eff}} \left(\nabla \boldsymbol{u}_h, \nabla \boldsymbol{v}_h\right) + \sigma \left(\boldsymbol{u}_h, \boldsymbol{v}_h\right) - \left(p_h, \nabla \cdot \boldsymbol{v}_h\right) \\ + \left(\nabla \cdot \boldsymbol{u}_h, q_h\right) + S_h \left[\left(\boldsymbol{u}_h, p_h\right), \left(\boldsymbol{v}_h, q_h\right)\right] \\ = \left(g, q_h\right) + G_h \left[\boldsymbol{v}_h\right], \end{aligned} \tag{13}$$

for all $(\boldsymbol{v}_h, q_h) \in \boldsymbol{V}_h \times Q_h$. In (13), the source term g is defined as in (4) using (6) and the approximate delta function (7), and we have introduced the so-called non-symmetric GLS stabilization and the grad-div stabilization terms

$$\begin{aligned} S_h \left[\left(\boldsymbol{u}, p\right), \left(\boldsymbol{v}, q\right)\right] &:= \alpha \sum_{\boldsymbol{T} \in \mathcal{T}_h} \frac{h_{\boldsymbol{T}}^2}{\nu} \left(\sigma \boldsymbol{u} + \nabla p, \sigma \boldsymbol{v} + \nabla q\right)_{\boldsymbol{T}} \\ &\quad + \delta \, \nu \left(\nabla \cdot \boldsymbol{u}, \nabla \cdot \boldsymbol{v}\right), \\ G_h \left[\boldsymbol{v}\right] &:= \delta \, \nu \left(g, \nabla \cdot \boldsymbol{v}\right), \end{aligned}$$

where α and δ are positive stabilization parameters, and $\nu = \mu_{\text{eff}} + \sigma \ell_{\boldsymbol{\Omega}}^2$, $\ell_{\boldsymbol{\Omega}}$ being a typical physical length scale of the problem, see [17].

4.2.2 Transient heat equation

In order to approximately solve the problem for the temperature field (11), we utilize the regularized Delta function (7) and define

$$\begin{aligned} c &:= \sum_{k=1}^{N^{\text{inj}}} \gamma \frac{Q_{w_{3D,k}^{inj}}}{H} \delta_{w_k^{inj}}^{r_\varepsilon}, \\ f &:= \sum_{k=1}^{N^{\text{inj}}} \gamma \frac{Q_{w_{3D,k}^{inj}}}{H} \delta_{w_k^{inj}}^{r_\varepsilon} T_{w_k^{\text{inj}}}. \end{aligned} \tag{14}$$

We discretize (11) in time via an implicit (backward) Euler scheme. Denoting with T^n the approximated temperature field at time t^n and with $\Delta t_n := t^n - t^{n-1}$ the time step, the time-discretized heat equation reads

$$\begin{aligned} aT^n + \Delta t_n \left(-d\Delta T^n + \boldsymbol{u} \cdot \nabla T^n + cT^n\right) \\ = aT^{n-1} + \Delta t_n f^n \quad \text{in } \widehat{\boldsymbol{\Omega}}. \end{aligned} \tag{15}$$

As next, we discretize (15) in space using a finite element method, seeking the solution in the space of continuous and piecewise linear functions:

$$\mathbb{T}_h := \left\{ s_h \in C^0(\overline{\widehat{\boldsymbol{\Omega}}}) \colon s_h|_{\boldsymbol{T}} \in \mathbb{P}_1 \left(\boldsymbol{T}\right), \forall \, \boldsymbol{T} \in \mathcal{T}_h \right\}.$$

The finite element formulation reads: Find $T_h^n \in \mathbb{T}_h$ with $T_h^n|_{\partial\widehat{\boldsymbol{\Omega}}} = T_0$ such that

$$\begin{aligned} a \left(T_h^n, s_h\right) + \Delta t_n \left(d \nabla T_h^n, \nabla s_h\right) \\ + \Delta t_n \left(\boldsymbol{u} \cdot \nabla T_h^n + cT_h^n, s_h\right) \\ = a \left(T_h^{n-1}, s_h\right) + \Delta t_n \left(f^n, s_h\right), \\ \forall s_h \text{ in } \mathbb{T}_h \text{ with } s_h|_{\partial\widehat{\boldsymbol{\Omega}}} = 0. \end{aligned} \tag{16}$$

Remark 5 (On the penalty parameter γ)
The penalty parameter γ in (14) *influences the time required to enforce a temperature equal to the injection temperature within the circular region of radius r_ε.*

5.1 Optimization of energy production

Based on the above described computational model, the goal of this work is to propose an efficient algorithm for computing the parameters describing deep geothermal installations (e.g., well locations) that maximize the net energy production – also called doublet/triplet/etc. capacity – subject to geological, ecological, and economic restrictions.

Let us assign to each well a pump efficiency $\varepsilon_{w^{(\star)}} \in (0, 1]$ and a recharge or discharge rate $Q_{w^{(\star)}}\,[\mathrm{m}^3/\mathrm{s}]$. The net energy $E_{\mathrm{net}}\,[\mathrm{J}]$ produced in the maximum operational time $t^L\,[\mathrm{s}]$ is given by

$$E_{\mathrm{net}} := \int_0^{t^L} \left(e_{\mathrm{prod}}\left(t\right) - e_{\mathrm{pump}}\left(t\right)\right) \mathrm{d}t, \tag{17}$$

where

$$e_{\mathrm{prod}}(t) = \rho_f C_f \left(\sum_{l=1}^{N^{\mathrm{prod}}} Q_{3D,w_l} T_l(t) - \sum_{k=1}^{N^{\mathrm{inj}}} Q_{3D,w_k} T_k(t) \right)$$

stands for the energy flux gained through the heat transfer, while

$$e_{\mathrm{pump}}(t) = \sum_{j=1}^{N^{\mathrm{prod}}+N^{\mathrm{inj}}} \frac{Q_{3D,w_j}}{\varepsilon_{w_j}} \left|\Delta p_{w_j}(t)\right|$$

denotes the energy flux that has to be invested in the operation of the pumps and represents energy losses. In e_{prod}, T_l and T_k stand for the temperatures at the wells l and k, while Δp_{w_j} denotes the pressure difference with respect to the ambience/reference pressure induced by the pump at the respective well.

Assuming that the lifetime interval $[0, t^L]$ is subdivided into N_t sub-intervals of equal length Δt, we approximate the net energy as

$$E_{\mathrm{net}} = \sum_{i=1}^{N_t} \Delta t \left(e_{\mathrm{prod}}\left(i\Delta t\right) - e_{\mathrm{pump}}\left(i\Delta t\right)\right). \tag{18}$$

The optimization problem consists then in finding the positioning of wells that maximizes the energy production E_{net}. Notice that E_{net} depends on the well locations $\{(x_{w^{(\star)}}, y_{w^{(\star)}})\}$ through the pressure and the temperature fields, as well as through the total operation time t^L (see Section 4.1.2).

The considered optimization problem for the multiple well placement aims at minimizing the pressure difference between injection and production wells while maximizing the time until the *thermal breakthrough* – the time at which the temperature at a production well drops below the formation temperature – takes place. After the occurrence of the thermal breakthrough, the temperature decline speed at the production wells is decisive for the resulting net energy.

Remark 6 (Constraint on the inter-well distance)
From the reservoir engineering viewpoint, a reasonable and economic prerequisite for any deep

geothermal installation is that the injection and production rates are chosen according to the given permeability structure of the targeted reservoir region such that energy can be extracted as long as possible, within the estimated scheduled operational time.

It is worthwhile noting that the distance, and thus the geometric parameters, between injection and production wells can only be varied within a reasonable range since sufficient hydraulic connectivity between injection and production wells should be practically guaranteed. Hence, when it comes to the optimization of the geothermal energy production by multiple wells, not only the optimal placement of the wells in the reservoir is searched for, but also the optimal distance relative to each other plays an important role for the different multiple well arrangements.

Remark 7 (Model limitations)
As described earlier, the employed non-matching immersed boundary method (Sections 4.0.2 and 4.1.3) incorporates the wells in the modeling domain. It provides a physically meaningful solution only starting from a distance r_ε (larger than the well radius) from the center of the well. Hence, pressure and fluid temperature cannot be exactly evaluated at the well boundary, yielding in practice slightly more pessimistic estimates for the net energy and the economic lifetime. On the other hand, it is reasonable to assume that this approximation does not have a significant influence on the simulation results for optimal placement. Related to the model dimension reduction, injection and production pressures used in the energy computation are evaluated at the level of the aquifer (i.e., bottomhole pressure (BHP), bottomhole temperature (BHT)). These pressures differ from the pump pressures at the ground level of the geothermal plant. Therefore, when computing the energy, we neglect the work needed to pump water from the surface to the bottomhole of the injection well and from the bottomhole of the production well up to the plant.

7.1 Validation and benchmarking of the numerical solver

The finite element library ParMooN has been used and validated in several publications, [48, 105], including fluid flow in porous media, [17]. The scope of this section is to assess the finite element solver and the accuracy of the immersed boundary method considering a setting particularly relevant for the problem of interest.

7.1.1 Fluid flow

We start with a simple one-well problem, considering the annular domain

$$\mathbf{\Omega} := \left\{(x,y) \in \mathbb{R}^2 \ : \ r_0^2 \leqslant x^2 + y^2 \leqslant r_1^2\right\} \tag{19}$$

with $r_0 := 0.2\,\mathrm{m}$ and $r_1 := 1000\,\mathrm{m}$, perforated by an injection well

$$w^{\mathrm{inj}} := \left\{(x,y) \in \mathbb{R}^2 \ : \ x^2 + y^2 \leqslant r_0^2\right\}$$

with boundary $\Gamma_{w^{\mathrm{inj}}} := \partial w^{\mathrm{inj}}$ (a circle of radius r_0).

For the immersed boundary approach, we introduce the extended domain

$$\mathbf{\Omega} \cup w^{\mathrm{inj}} = \left\{(x,y) \in \mathbb{R}^2 \ : \ x^2 + y^2 \leqslant r_1^2\right\}$$

and use the discrete Dirac delta function (7) with $r_\varepsilon = 50\,\mathrm{m}$. Hence, the numerical solution is expected to behave as the physical one at a distance from the origin larger than $50\,\mathrm{m}$.

In order to assess the capability of the finite element solver in approximating the solution near the wells, we consider porous media flow described by the Darcy equations (groundwater flow equations), i.e., $\mu_{\text{eff}} = 0$, with non-homogeneous Dirichlet boundary conditions for the velocity imposed on $\Gamma_{w^{\text{inj}}}$ and homogeneous pressure boundary conditions on the outer boundary, i.e.,

$$\begin{aligned} \boldsymbol{u} \cdot \boldsymbol{n} &= U_{w^{\text{inj}}} \qquad \text{on } \Gamma_{w^{\text{inj}}}, \\ p &= 0 \qquad\quad \text{on } \partial\boldsymbol{\Omega} \setminus \Gamma_{w^{\text{inj}}}, \end{aligned} \tag{20}$$

for some $U_{w^{\text{inj}}} \in \mathbb{R}$ and vanishing source terms. In this setting, problem (1a)-(1b) admits the analytic solution

$$\begin{aligned} \boldsymbol{u}^{sol}(x,y) &= \frac{U_{w^{\text{inj}}} r_0}{x^2+y^2} \begin{pmatrix} x \\ y \end{pmatrix}, \\ p^{sol}(x,y) &= \sigma U_{w^{\text{inj}}} r_0 \log\left(\frac{r_1}{\sqrt{x^2+y^2}} \right) \end{aligned} \tag{21}$$

(notice that the velocity and the pressure fields are well defined only in the physical domain $\boldsymbol{\Omega}$). For the numerical tests we take $\mu = 0.0003\,\text{kg/m s}$, $K = 3 \cdot 10^{-12}\,\text{m}^2$, yielding $\sigma = 10^8\,\text{kg/m}^3\,\text{s}$, and $\ell_{\boldsymbol{\Omega}} = 50\,\text{m}$. Moreover, we use $Q_{3D,w^{\text{inj}}} = 100\,\text{l/s}$, calculate $U_{w^{\text{inj}}} = \frac{Q_{3D,w^{\text{inj}}}}{2\pi r_0 H}$ as described in (2), and use the remaining parameters as given in Table 6. We use a triangular mesh containing about 17500 vertices and 35000 triangles, with diameters between $h_{\min} = 6.85\,\text{m}$, and $h_{\max} = 27.90\,\text{m}$.

In Figure 7 we compare the exact solution $\left(\boldsymbol{u}^{sol}, p^{sol}\right)$, which is defined only outside the well with radius r_0, i.e. in $\boldsymbol{\Omega}$, with the numerical solution obtained via the immersed boundary method with $r_\varepsilon = 50\,\text{m}$, i.e., solving the problem (13) on $\widehat{\boldsymbol{\Omega}}$. We visualize one half of a circular, centered cutout of radius $100\,\text{m}$ from the respective domain ($\boldsymbol{\Omega}$ and $\widehat{\boldsymbol{\Omega}}$).

The tests confirm that the resulting velocity and pressure fields approximate well the exact solution for radii larger than or equal to r_ε. In particular, the pressure isolines (for the immersed method) fit well with those for the exact solution.

7.1.2 Heat transport

As next step, we assess the effect of the penalty-based method, employed to impose the Dirichlet boundary condition on the boundary of the wells for the heat transport problem (11), on the resulting temperature field. To that end, we consider the single well domain $\boldsymbol{\Omega}$ defined in (19) and the advective field $\boldsymbol{u}^{sol}$ defined in (21).

The temperature is prescribed at the inner circle, while at the outer circle we impose a homogeneous Neumann boundary condition. All remaining parameters in (9) and (11) are chosen as described in Table 6.

We compare (i) the temperature field obtained imposing stronlgy the Dirichlet boundary condition at the well boundary as in (9) and (ii) the temperature field computed via the penalty-based immersed boundary method (16).

In the following computations we use for $\boldsymbol{\Omega}$ a mesh with 20 nodes on $\Gamma_{w^{\text{inj}}}$ and 160 nodes on the outer circular boundary, resulting in 24022 triangles, $h_{\min} = 0.064\,\text{m}$, $h_{\max} = 55.40\,\text{m}$, and 12100 mesh nodes. For $\widehat{\boldsymbol{\Omega}}$ a mesh with 20 nodes, uniformly distributed along the artificial well boundary with radius $r_\varepsilon = 50\,\text{m}$ is considered instead, resulting in a coarser grid with 8657 triangles, $h_{\min} = 13.75\,\text{m}$, $h_{\max} = 55.49\,\text{m}$ and 4409 mesh nodes.

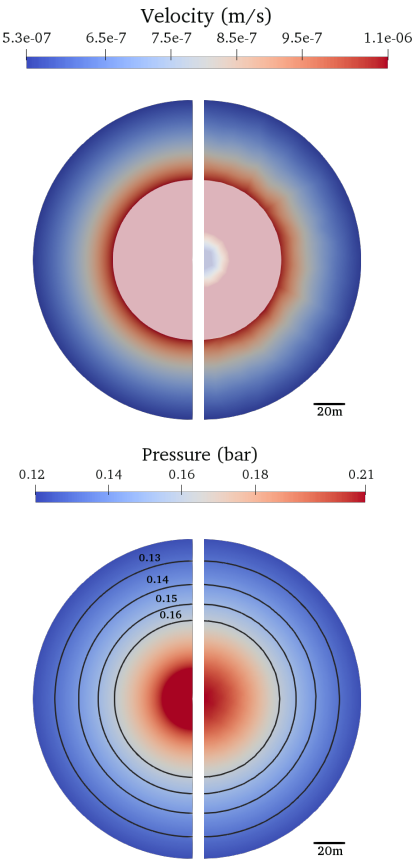

Figure 7: Velocity field (top) and pressure field with selected contours (bottom) in a centered cutout of radius $100\,\mathrm{m}$, resulting from a single injection well operated with a constant flow rate of $100\,{}^{\mathrm{l}}/_{\mathrm{s}}$. The artificial well has a higher transparency than the rest of the modeling domain (top). The exact solution $\boldsymbol{u}^{sol}$ respectively p^{sol} is shown in the left halves, while the velocity field respectively pressure field obtained with the immersed method is depicted in the right halves.

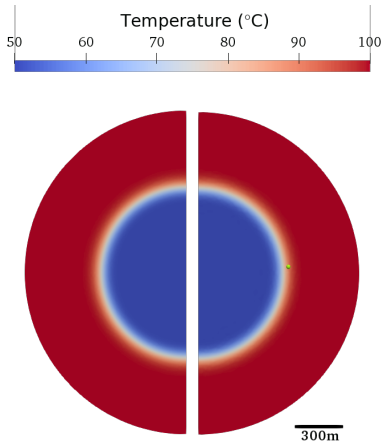

Figure 8: Temperature distribution at simulation time $t = 50$ years in the annular domain resulting from a single injection well operating with $100\,{}^{\mathrm{l}}/_{\mathrm{s}}$ constant flow rate. The left half is the solution obtained prescribing Dirichlet boundary conditions ($T = 50\,^{\circ}\mathrm{C}$) on the well boundary, while the right half of the plot shows the solution using the immersed boundary approach. The green point has the coordinates $(560, 40)\,\mathrm{m}$.

The results displayed in Figures 8-9 compare the temperature fields after 50 years (Fig. 8) and the temperature evolution at a specified point (Fig. 9). They show good agreement between the solutions of the approaches (i) and (ii). It shall be mentioned that the progressing cooling front (Figure 9) computed with the penalty method is slightly faster than the one obtained with classically imposed Dirichlet boundary conditions (the difference is about 0.5 years). This effect is due to the fact that in the penalty approach, the inner temperature is immediately imposed at the radius r_ε, which is larger than the actual physical well, whereas in the case of strongly imposed Dirichlet boundary condition the cold water thermal front reaches r_ε only after few iterations. On the other hand, since this artifact is present in all considered geometrical configurations, we assume that it only marginally affects the result of the forthcoming comparative optimization studies – provided that r_ε is sufficiently small.

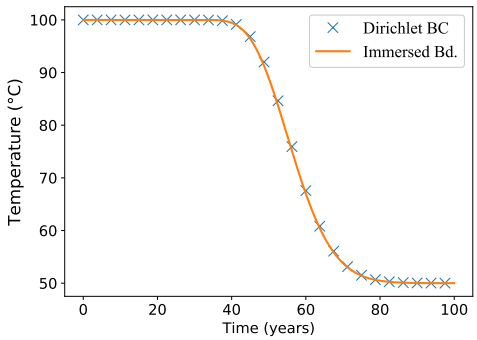

Figure 9: Evolution of temperature at the point $(x, y) = (560, 40)\,\mathrm{m}$ in the simulation of an annular domain and a single injection well operating with $100\,{}^{\mathrm{l}}/_{\mathrm{s}}$ constant flow rate. We compare the solution with Dirichlet boundary conditions (blue crosses) with the immersed boundary one (orange line).

7.1.3 Single doublet: mesh- and boundary condition-independence studies

The purpose of this last validation step is to perform an extensive preliminary study concerning the influence of the spatial and temporal discretization, as well as the boundary conditions. The model setup consists of a single doublet, i.e., one production and one injection well with fixed inter-well distance $1000\,\mathrm{m}$ and flow rates $Q_{w^{\mathrm{prod}}} = Q_{w^{\mathrm{inj}}} = 100\,{}^{\mathrm{l}}/_{\mathrm{s}}$. All remaining physical parameters are defined as in Table 6.

$\lvert\widehat{\Omega}\rvert\ [\mathrm{km}^2]$ (DOFS)	3×3 (43657)	5×5 (44203)	8×8 (46042)	10×10 (47549)	15×15 (52536)
$\Delta t = 1\mathrm{a}$	$55 \xrightarrow{-5.46\%} \downarrow +2.73\%$	$52 \xrightarrow{-1.92\%} \downarrow +2.89\%$	$51 \xrightarrow{0\%} \downarrow +2.94\%$	$51 \xrightarrow{0\%} \downarrow 2.94\%$	$51 \downarrow +1.96\%$
$\Delta t = \frac{1}{2}\mathrm{a}$	$56.5 \xrightarrow{-5.31\%} \downarrow +1.77\%$	$53.5 \xrightarrow{-1.87\%} \downarrow +1.40\%$	$52.5 \xrightarrow{0\%} \downarrow +1.91\%$	$52.5 \xrightarrow{-0.95\%} \downarrow +0.95\%$	$52 \downarrow +1.44\%$
$\Delta t = \frac{1}{4}\mathrm{a}$	$57.5 \xrightarrow{-5.65\%} \downarrow +0.57\%$	$54.25 \xrightarrow{-1.38\%} \downarrow +0.61\%$	$53.5 \xrightarrow{-0.94\%} \downarrow +0.62\%$	$53 \xrightarrow{-0.47\%} \downarrow +1.09\%$	$52.75 \downarrow +0.95\%$
$\Delta t = \frac{1}{12}\mathrm{a}$	$57.83 \xrightarrow{-5.62\%}$	$54.58 \xrightarrow{-1.37\%}$	$53.83 \xrightarrow{-0.46\%}$	$53.58 \xrightarrow{-0.62\%}$	53.25

Table 1: Specific lifetimes in years for varying domain size (in km^2) and time step length (in years). Cells marked in green indicate a total variation less than 2% with respect to the subsequent temporal refinement and domain size increase. All quantities are rounded to two decimal places.

The wells are placed horizontally and vertically centered in a computational domain $\widehat{\Omega}$ of varying size, which is discretized with a non-uniform triangular mesh. A subregion of size $2.4 \times 1.4\,\mathrm{km}^2$ contains

the doublet, is discretized with computational meshes of increasing resolution, and embedded in a coarser mesh. We monitor the specific lifetime of the doublet (see Section 4.1.2), varying the size of the smallest triangles, the time step size and the size of the domain (i.e., the distance between the wells and the outer boundary of the modeling domain). The threshold temperature at the production well is defined as $T_{\mathrm{quit}} = 90\,^{\circ}\mathrm{C}$.

Table 1 summarizes the results of the investigation concerning the time step length and the distance to the outer boundary of the modeling domain. In particular, it can be seen that the boundary has a negligible effect on the specific lifetime of the doublet whenever it has a distance of about $\geqslant 3.5\,\mathrm{km}$ from the wells which corresponds here to a domain size $8 \times 8\,\mathrm{km}^2$ or larger. Concerning the time discretization, results become almost independent (variation of less than $\approx 1\%$) of the chosen time step for values below 3 months.

In order to assess the influence of the spatial discretization, we consider in accordance with the previous results in Table 1 the case of a domain of size $10 \times 10\,\mathrm{km}^2$ and a time step length equal to 3 months. In this configuration, we refine the mesh in the region of interest (centered and of size $2.4 \times 1.4\,\mathrm{km}^2$), considering local element sizes between approximately $3\,\mathrm{m}$ and $50\,\mathrm{m}$, and monitor in each case the specific lifetime of the doublet.

The results compiled in Table 2 show that the mesh width in the active region has an impact on the specific lifetime. Too coarse meshes (row 1) seem to yield a significantly overestimated specific lifetime but differences for the smaller mesh-sizes are relatively small. A mesh size of less than $28\,\mathrm{m}$ already assures a variation slightly below 1%. Note that the mesh size should be chosen in dependence of the artificial well diameter, which is $2r_{\varepsilon}$.

Mesh Size $(h_{\min},\, h_{\max})$ $[\mathrm{m}]$	Specific Lifetime $[\mathrm{a}]$
$(51.0751, 259.815)$	57.75 $\downarrow -8.66\%$
$(28.2705,\ 267.206)$	52.75 $\downarrow +0.47\%$
$(12.8648,\ 267.206)$	53 $\downarrow 0\%$
$(6.14902,\ 262.21)$	53 $\downarrow +0.94\%$
$(2.93729,\ 262.183)$	53.5

Table 2: Specific lifetimes in years (time step equals to 3 months) for refinement of the subdomain $2.4 \times 1.4\ \mathrm{km}^2$ (characterized by $h_{\min}$) in the $10 \times 10\ \mathrm{km}^2$ modeling domain. Green color visualizes less than 1% variation with respect to the subsequent refinement.

Finally, we use the information gained in the previous studies to set up and simulate an appropriate doublet configuration. Figures 10, 11, and 12 show the simulation results concerning velocity, pressure, and temperature fields at the end of the specific lifetime in the active subregion of size $2.4 \times 1.4\,\mathrm{km}^2$ with mesh size $h = 6.15\,\mathrm{m}$ ($h = 262.21\,\mathrm{m}$ elsewhere in the modeling domain), time step length $\Delta t = 3$ months, and modeling domain size $10 \times 10\,\mathrm{km}^2$. The distance between injection well (left) and production well (right) is equal to $1000\,\mathrm{m}$, the permeability is constant with value $K = 3 \cdot 10^{-12}\,\mathrm{m}^2$ and thermal dispersion has been omitted. All parameters that were not defined in this subsection are set as described in Table 6.

The arrows in the visualization of the velocity (Figure 10) indicate that the flow is directed from the injection well (left) towards the production well (right). Due to the homogeneity of the domain and the same flow rates at both wells, the pressure (Figure 11, left) is symmetric with respect to the isoline $0\,\mathrm{bar}$ (except for the sign). The pressure build-up and draw-down (also called *groundwater impression and depression cones*) are shown in Figure 11 (right) and reveal a steep gradient in the vicinity of the wells only.

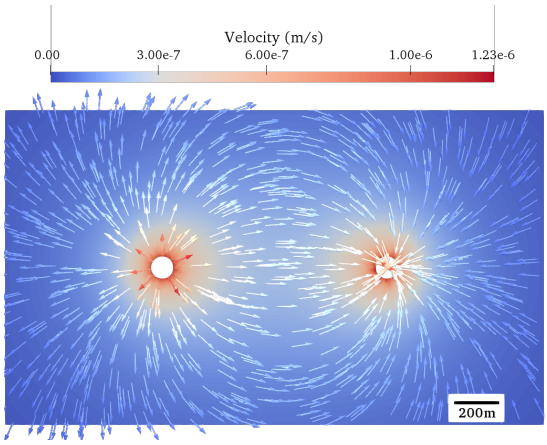

Figure 10: Magnitude of the velocity with unscaled arrows for the doublet setup with injection and production rate equal to $100\,{}^{1}\!/\!_{\mathrm{s}}$.

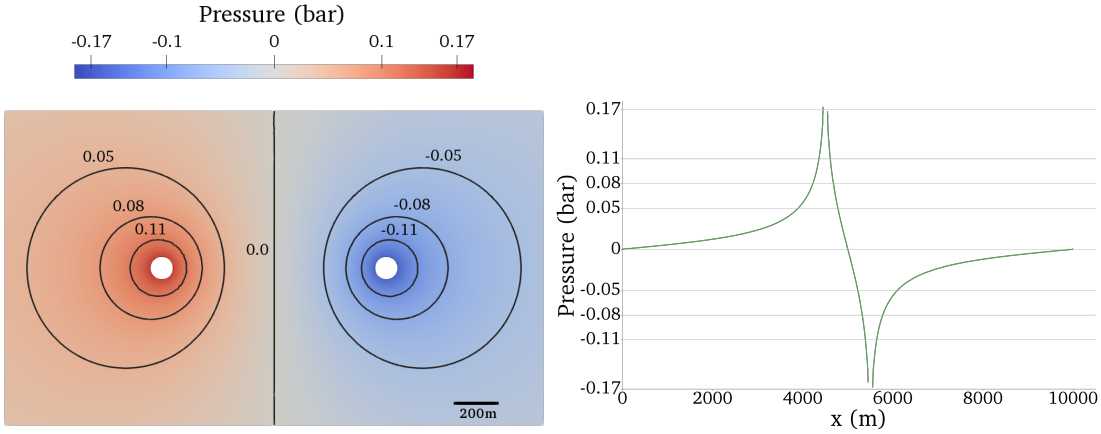

Figure 11: Simulation results concerning a doublet setup with injection and production rate equal to $100\,{}^{1}\!/\!_{\mathrm{s}}$. Left Panel: Pressure with isolines. Right panel: Pressure along the direct line connecting the injection and production well.

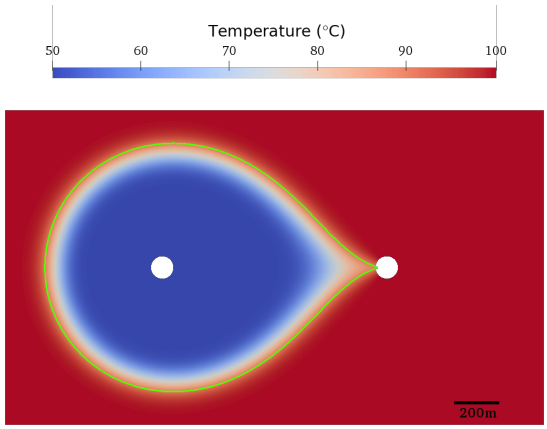

Figure 12: Simulation results concerning a doublet setup with injection and production rate equal to $100\,{}^{1}\!/\!_{\mathrm{s}}$, injection temperature $50\,^{\circ}\mathrm{C}$. Temperature distribution after 53 years of operation with an isoline (green) highlighting $90\,^{\circ}\mathrm{C}$ isotherm.

The cold water plume after 53 years of constant doublet operational scheme is surrounded by the contour line (green) referring to the minimum operation temperature of $90\,^{\circ}\mathrm{C}$ and has the typical tear drop shape towards the production well, see Figure 12.

8 Model setups

8.1 Case studies

The different configurations analyzed in this work are inspired by previous geothermal multi-well arrangements considered in different geothermal projects worldwide for several purposes (see, e.g., [71, 106]. From the reservoir management viewpoint, another important motivation behind our study constitutes the strikingly dynamic geothermal development for district heating in the Greater Munich region and related urgent questions. To this purpose, various geothermal reservoir settings similar to the ones encountered in the Upper Jurassic carbonates in the Greater Munich region are implemented and simulated within the proposed optimization framework. In particular, we focus on geothermal multiple doublet arrays (*lattice*) and smart multi-well *hexagonal* configurations.

An arrangement similar to the hexagonal multi-well configuration is currently being implemented around a major fault damage zone at the geothermal site Heizkraftwerk Süd in the Schäftlarnstraße (Munich) in the form of multi-lateral wells, which are drilled from one common surface location. Future multi-well arrangements are planned for the near future in the city of Munich, hence the considered configurations may serve as a starting point for further analyses on smart geothermal multi-well arrangements in mega cities, where the heat demand is substantial and an evident lack of space problem is existing [24, 56, 103].

In both cases, we investigate different simulation scenarios characterized by:

- heterogeneous geological conditions,
- boundary and initial conditions (temperature),
- production and injection wells (and flow rates).

8.1.1 Lattice

The lattice configuration is composed of doublet arrays, consisting of 8 injection and 8 production wells, arranged in form of a 4 rows $\times$ 4 columns lattice. In each row, two doublets are placed, where injection and production sites appear staggered: the rows 1 and 3 start with a production well, whereas the rows 2 and 4 start with an injection well (see Figure 13, left). The same constant flow rates of $100\,{}^{\mathrm{l}}/_{\mathrm{s}}$ are imposed for all wells, i.e., in total $1600\,{}^{\mathrm{l}}/_{\mathrm{s}}$.

Different scenarios are generated varying the permeability structure, the temperature initial and boundary conditions, and the control variables of the optimization procedure.

Permeability structure. Firstly, we consider a horizontally varying permeability structure with two different permeabilities. This is intended to resemble two different carbonate facies such as bedded

and reef facies as typically encountered in the Upper Jurassic carbonates in the Munich region

$$K = \begin{cases} 3 \cdot 10^{-15}\,\mathrm{m}^2, & \text{for } 5.5\,\mathrm{km} \leq x \leq 7\,\mathrm{km}, \\ 3 \cdot 10^{-15}\,\mathrm{m}^2, & \text{for } 8.5\,\mathrm{km} \leq x \leq 9\,\mathrm{km}, \\ 3 \cdot 10^{-12}\,\mathrm{m}^2, & \text{elsewhere}, \end{cases} \tag{22}$$

as indicated in Figure 13, left.

Aquifer temperature. Secondly, we distinguish between (i) constant initial and boundary temperature conditions and (ii) a dipping aquifer with linearly varying initial and boundary temperature conditions.

In order to asses the impact of geometrical parameters of the lattice arrangement on the net energy, different scenarios with varying control variables in particular for heterogeneous temperature and permeability fields are examined. For each case, we seek the optimal position of the wells with respect to the produced net energy (equation (18)).

Multi-well configurations. The degrees of freedom for the search of optimized configurations (here concerning the movement of the wells) are referred to as the control variables. In a first scenario, we fix the position of the lattice center at the center of the domain and consider variations of the *lattice size* (i.e., the distance between closest wells) and rigid rotations. Thereby, the lattice size is allowed to vary between $500\,\mathrm{m}$ and $1414\,\mathrm{m}$, while the *rotation angle* cannot exceed 180° due to symmetry. In a second scenario, we fix the lattice size equal to $600\,\mathrm{m}$, allowing a rigid rotation in $[0^\circ, 180^\circ]$ and a rigid horizontal displacement with a maximal absolute value of $1221\,\mathrm{m}$ with respect to the initial position. The considered setups are summarized in Table 3.

Scenario	Permeability	Initial Temp.	Control variables
LC	Het. eq. (22)	Constant, eq. (25)	lattice size, rotation angle
L1	Het. eq. (22)	Linear, eq. (26)	lattice size, rotation angle
L2	Hom. ($K = 3 \cdot 10^{-12}\,\mathrm{m}^2$)	Linear eq. (26)	x-translation, rotation angle
L3	Het. eq. (22)	Linear, eq. (26)	x-translation, rotation angle

Table 3: Permeability structures, initial temperature distributions, and control variables for the optimization in the considered lattice scenarios (doublet arrays). Lattice size refers to the variation of the lattice dimensions, whereas position (x) and rotation angle refer to the translation forwards and backwards along the x-axis and rotation with respect to the lattice center, respectively.

8.1.2 Hexagon

In this case we consider an equilateral hexagonal multi-well structure embedded in heterogeneous modeling domains. The heterogeneities in the reservoirs are characterized as fault damage zones, delimited by two lines (see Figure 13, right). We seek for the optimal configuration varying the radius of the hexagon between $500\,\mathrm{m}$ and $2800\,\mathrm{m}$ and rigidly rotating the hexagon up to 180° with respect to its center, which is also the center of the modeling domain.

The different scenarios are described below and summarized in Table 4.

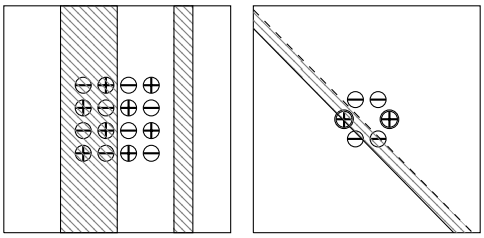

Figure 13: Sketch of the $6 \times 6\,\mathrm{km}^2$ (centered) subdomain for the configurations lattice (LC, left) and hexagon (H_{I2P4}, right). The dashed line confining the fault damage zone for the hexagon is variable in its distance with respect to the solid line. $\oplus$ indicates injection wells, $\ominus$ indicates production wells, patterned and plain regions indicate two different permeabilities.

Permeability structure. We consider two cases, depending on whether the center of the hexagon is located within the fault damage zone or outside of it. In the first case (hexagon center within the damage zone), we consider a damage zone with a width (denoted by $\mathrm{width}^{\mathrm{dz}}$) of 400m, which is formally defined by the lines passing through the two domain points: $(a_1, 0)$ and $(0, a_1)$ (lower line in Figure 13, left) and $(a_2, 0)$ and $(0, a_2)$ (upper line in Figure 13, left). We use $a_1 = 13717.66\,\mathrm{m}$ and $a_2 = 14282.3\,\mathrm{m}$.

In the second setup (hexagon center outside the damage zone), we consider fault damage zones of different widths, i.e.,

$$\mathrm{width}^{\mathrm{dz}} \in \{100, 200, 300, 400\}\ \mathrm{m}.$$

The setups are obtained considering the lines passing through the points $(a_3, 0)$ and $(0, a_3)$, and $(a_3 + \sqrt{2}\,\mathrm{width}^{\mathrm{dz}}, 0)$ and $(0, a_3 + \sqrt{2}\,\mathrm{width}^{\mathrm{dz}})$, with $a_3 = 13400\,\mathrm{m}$.

We further distinguish two different permeability structures: (I) with a weakly healed fault damage zone:

$$K = \begin{cases} 3 \cdot 10^{-12}\,\mathrm{m}^2, & \text{fault damage zone,} \\ 3 \cdot 10^{-11}\,\mathrm{m}^2, & \text{elsewhere,} \end{cases} \tag{23}$$

and (II) with a hydraulically active fault damage zone (i.e., a *leak fault*):

$$K = \begin{cases} 3 \cdot 10^{-12}\,\mathrm{m}^2, & \text{fault damage zone,} \\ 3 \cdot 10^{-15}\,\mathrm{m}^2, & \text{elsewhere.} \end{cases} \tag{24}$$

Multi-well configurations. In addition, the following scenarios are considered:

$\mathrm{H}_{(3,3)}$: 3 injection and 3 production wells (alternated) along the hexagon and the flow rates $100\,\mathrm{l/s}$ (for all wells),

$\mathrm{H}_{(4,2)}$: 4 injection and 2 production wells, injection rates $Q_{w^{\mathrm{inj}}} = 50\,\mathrm{l/s}$, production rates $Q_{w^{\mathrm{prod}}} = 100\,\mathrm{l/s}$,

$\mathrm{H}_{(2,4)}$: 2 injection and 4 production wells, injection rates $Q_{w^{\mathrm{inj}}} = 100\,\mathrm{l/s}$, production rates $Q_{w^{\mathrm{prod}}} = 50\,\mathrm{l/s}$.

The last setup is additionally considered on the one hand with a permeable damage zone of width $400\,\mathrm{m}$ containing the center of the hexagon (permeability defined in (24)) and on the other hand with a slightly healed damage zone (permeability defined in (23)) of width $200\,\mathrm{m}$.

Scenario	Permeability	$\mathbf{width}^{dz}$	Wells	Total flow rate
$\mathsf{H}_{(3,3)}$	Eq. (24)	$400\,\mathrm{m}$	$\oplus\ominus\oplus\ominus\oplus\ominus$	$600\,\mathrm{l/s}$
$\mathsf{H}_{(4,2)}$	Eq. (24)	$400\,\mathrm{m}$	$\oplus\oplus\ominus\oplus\oplus\ominus$	$400\,\mathrm{l/s}$
$\mathsf{H}_{(2,4)}1$	Eq. (24)	$400\,\mathrm{m}$	$\oplus\ominus\ominus\oplus\ominus\ominus$	$400\,\mathrm{l/s}$
$\mathsf{H}_{(2,4)}2$	Eq. (24)	$400\,\mathrm{m}$ (centered)	$\oplus\ominus\ominus\oplus\ominus\ominus$	$400\,\mathrm{l/s}$
$\mathsf{H}_{(2,4)}3$	Eq. (23)	$200\,\mathrm{m}$ (healed)	$\oplus\ominus\ominus\oplus\ominus\ominus$	$400\,\mathrm{l/s}$

Table 4: Permeability structures (including damage zone widths), well types along the hexagon (counter-clockwise, starting from the positive x-axis), and corresponding total flow rates for the considered hexagonal multi-well configurations. $\oplus$ indicates injection wells, while $\ominus$ stands for production wells.

8.2 Computational domain

The conceptual 2D model of the confined and saturated aquifer comprises an area of a square, the size of which is defined in order to minimize the influence of the boundary conditions on the computational results, according to the results of the preliminary numerical study conducted in Section 7.1.3.

Namely, we consider a domain of size $14 \times 14\,\mathrm{km}^2$ and an *active region* (with increased mesh resolution) of $6 \times 6\,\mathrm{km}^2$, such that a distance of $4\,\mathrm{km}$ is assured between the active region and the boundary. The domain is discretized with a non-uniform triangular mesh with characteristic mesh size of approximately $6\,\mathrm{m}$ in the *active region* (see Section 7.1.3). Outside the *active region*, the mesh is gradually coarsened, reaching a maximum element size of approximately $262\,\mathrm{m}$ near the boundary (see also Table 5).

It is worth noticing that the computational finite element mesh is generated only once at the beginning of the computational procedure and it is not updated at each optimization (when repositioning the wells). This aspect constitutes an important advantage of this numerical framework. Especially when computing numerous scenarios of multiple well configurations for a well placement optimization with finite element methods, computationally expensive and time consuming re-meshing procedures would be otherwise required. The time discretization is chosen based on the simulation results described in Table 1, having a constant time step length $\Delta t = 3$ months.

Modeling domain size	$14 \times 14\,\mathrm{km}^2$
Subdomain with enhanced resolution	$6 \times 6\,\mathrm{km}^2$
Smallest element diameter ($h_{\min}$)	$5.9\,\mathrm{m}$
Largest element diameter ($h_{\max}$)	$281.8\,\mathrm{m}$
# Nodes of the spatial mesh	547200
Time step length	3 months

Table 5: Mesh parameters used in the simulations.

8.3 Model parameters

We consider open hydraulic boundary conditions, i.e. boundary pressure in (3) as $P = 0\,\mathrm{Pa}$, so that all pressure values are computed with respect to the pressure at the depth of the aquifer, where the reference (datum) is set.

For the energy balance equation (11), which describes the spatio-temporal evolution of the temperature field, we set initial and boundary conditions according to the depth of the aquifer and corresponding natural geothermal conditions in conduction-dominated hot sedimentary aquifers. Specifically, the boundary conditions for the temperature field are based on the initial temperature distribution that mimics a temperature gradient of approximately $30\,^{\circ}\mathrm{C}/\mathrm{km}$ as described in Section 2. In particular for the case of aquifers that extend horizontally, assuming a constant depth of approximately $3\,\mathrm{km}$ below surface and a surface temperature of $10\,^{\circ}\mathrm{C}$, we set

$$\begin{aligned} T(0,\boldsymbol{x}) &= 100\,^{\circ}\mathrm{C}, \quad \text{for } \boldsymbol{x} \in \widehat{\boldsymbol{\Omega}}, \\ T(t,\boldsymbol{x}) &= 100\,^{\circ}\mathrm{C}, \quad \text{for } t > 0,\ \boldsymbol{x} \in \partial\widehat{\boldsymbol{\Omega}}\,. \end{aligned} \tag{25}$$

For the case of a dipping aquifer, we consider a temperature distribution that is constant in time and varies in space linearly along the boundary, such that

$$T(t,x,y) = \begin{cases} 100\,^{\circ}\mathrm{C}, & \text{for } x = 0\,\mathrm{km}, \\ 130\,^{\circ}\mathrm{C}, & \text{for } x = 14\,\mathrm{km}\,. \end{cases} \tag{26}$$

Note that this corresponds to a difference in depth of about $1\,\mathrm{km}$ in the horizontal direction.

The parameters used in the numerical simulations are summarized in Table 6.

9 Simulation results

9.1 Optimization parameters

The simulations have been performed solving the finite element problems (13) and (16) with the open source finite element library ParMooN [105], while the routines for the solution of the optimization problem related to the net energy (18) have been implemented using the open-source library NLopt [60]. NLopt supports a large variety of derivative-free optimization algorithms and, a priori, it can be hard to select the best choice for the considered problem, [89]. In our numerical investigation, we performed a detailed study of one global (DIRECTL, DIviding RECTangles algorithm Locally-biased, [47]) and two local (COBYLA, NEWUOA) optimization algorithms. This revealed that the local variants might converge faster but at the same time they might be trapped in a local minimum, i.e., not yielding a similarly optimal (with respect to the functional value) result at the global level. Therefore, in the numerical results presented in this section we show only the outcome of the global optimization algorithm DIRECTL. This is a deterministic search algorithm based on decomposing the search domain into hyperrectangles and using successive refinement.

The computational meshes have been generated using Gmsh, [49], which is an open source mesh generator. For the visualization of the simulation results, the post-processing tool ParaView [6] (open source) has been employed.

In all the considered setups we assume that the injection and production rates (Q_{inj}, Q_{prod}), the injection and production pressures (Δp^{inj}, Δp^{prod}), as well as the injection temperature T^{inj} do not depend on time. For each case, we performed 40 optimization steps and visualize the configuration of the optimization step that yielded the maximum net energy. If it is not explicitly stated otherwise, this will be the final optimization step. Let us note that an adequate number of optimization steps cannot be determined a priori in a theoretical manner. Instead it has to be chosen heuristically in accordance with the time frame for the simulation and the desired accuracy of the result. In general, an increase

Notation	Unit	Parameter Name	Lattice	Hexagon
$\mu_{\text{eff}} = \mu$	$\mathrm{kg}/\mathrm{m\,s}$	viscosities	0.0003	
$\mathbb{K}$	m^2	permeability	$\in 3 \cdot \{10^{-11}, 10^{-12}, 10^{-15}\}$	
H	m	aquifer thickness	300	
Q_{inj}, Q_{prod}	l/s	injection, production flow rates	100	$\in \{50, 100\}$
r_w	m	well radius	0.2	
t^L	a	maximum lifetime	80	
ϕ	-	porosity	0.28	
ρ_f	kg/m^3	fluid/brine density	1050	
C_f	$\mathrm{J}/\mathrm{kg\,K}$	fluid/brine heat capacity	4200	
ρ_s	kg/m^3	rock density	2650	
C_s	$\mathrm{J}/\mathrm{kg\,K}$	rock heat capacity	730	
λ_s	$\mathrm{J}/\mathrm{K\,m\,s}$	thermal conductivity (rock)	2.7	
λ_f	$\mathrm{J}/\mathrm{K\,m\,s}$	thermal conductivity (fluid/brine)	0.7	
α_L	m	longitudinal dispersion coefficient	5	
α_T	m	transversal dispersion coefficient	0	
T_{inj}	K	injection temperature	$323.15\ (= 50\,^\circ C)$	
T_0	K	aquifer/formation temperature	$373.15\ (=100\,^\circ C)$/linear	
T_{quit}	K	minimum production temperature	$363.15\ (= 90\,^\circ C)/-10\%$	
ε	-	pump efficiency	0.6	
α	-	stabilization parameter (GLS)	1	
δ	-	stabilization parameter (grad-div)	0.1	
$\ell_{\mathbf{\Omega}}$	m	characteristic length	300	
γ	-	penalty for temperature BC	100	
r_ε	m	artificial well radius (IBM)	50	
N_O	-	optimization steps	40	

Table 6: Top table: Petrophysical properties of the reservoir rock, fluid mechanical properties, reservoir dimensional parameters, and operational parameters used in the simulations, partly taken from [32, 106]. Bottom table: Numerical parameters used in the simulations.

of effort in the sense of more optimization steps has to be expected to enhance the optimality of the resulting controls. The choice of the number of optimization steps is particularly delicate if the behavior of the optimization functional (the objective function) cannot be classified as convex, having a global minimum, and/or being smooth.

The stopping criterion for the temperature simulation (in each optimization step) is twofold: On the one hand, the maximum production time is restricted to 80 years. On the other hand, the simulation stops whenever the specific lifetime is reached (see Section 4.1.2). The threshold temperature T_{quit} is defined based on a 10% temperature reduction with respect to the initial aquifer temperature. Due to the model approach (the non-matching immersed boundary method, see Section 4.2) the production temperatures at measurement points along the concentric circle of radius r_ε (enclosing the well) are utilized. For the sake of visibility of the active modeling domain defined in Subsection 7.1.3, the velocity, pressure, and temperature fields will be only shown within a centered $6 \times 6\,\mathrm{km}^2$ subdomain, which is in line with the allowed variation in the control variables (lattice size/hexagon radius, translation, and rotation).

It is worth noting that for each configuration tested, the velocity and the pressure fields remain constant over the entire simulation time. This is the result of the assumptions made in the formulation of the physical problem.

Generally, the symbol $\oplus$ is utilized to refer to an injection well, while $\ominus$ represents a production well.

9.2 Lattice configurations

9.2.1 Optimal placement and net energy

In Figure 14 we plot for each of the lattice scenarios introduced in Subsection 8.1.1 (see also Table 3) the resulting net energy over the optimization steps.

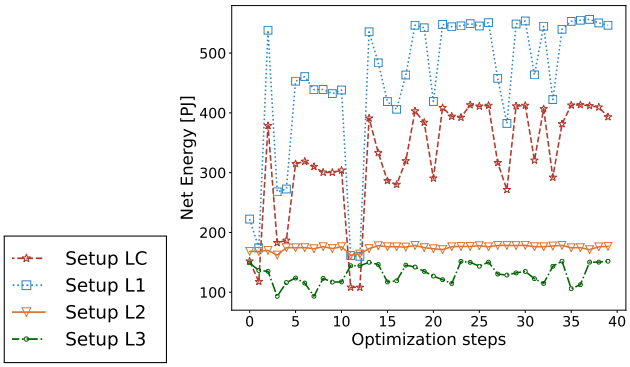

Figure 14: Net energy for 40 optimization steps with the global optimization algorithm DIRECTL for the four different lattice scenarios (Table 3).

The results show the strong impact of the inter-well distance (lattice size) on the extracted energy. In fact, including the variation of the lattice size as optimization variable (setups LC and L1) allows to increase the obtained energy by approximately up to 300% with respect to the cases L2 and L3, where the lattice size is kept fixed.

The net energy for LC is generally smaller than that for L1, which can be explained by the larger average temperature of the considered aquifer domain in L1. The net energy for the setups with fixed lattice size (L2 and L3) is more robust with respect to a variation of their controls. In particular, the homogeneous setup L2 has an almost constant energy level which is larger than the slightly varying energy associated with its heterogeneous (with partly lower permeability) version L3.

Finally, the simulation results for the scenario L1 show that alone for a $6 \times 6\,\mathrm{km}^2$ area covered with an optimized 4×4 doublet array structure operating with $100\,{}^{\mathrm{l}}/_{\mathrm{s}}$, around $219\,\mathrm{MW_{th}}$ ($\approx 553\,\mathrm{PJ}$ in 80 years operation time) can be developed for district heating. Concerning the planned heat contribution of $400\,\mathrm{MW_{th}}$ from geothermal energy in the case of the city of Munich, this result suggests that such optimized doublet arrays are capable to reach this goal.

9.2.2 Simulation results in the optimal configurations

The optimization algorithm consists of simulating multiple scenarios using an appropriate sampling of the control variable space. Depending on the considered setup, the inter-well distance (lattice size), the translation in the direction of the *x*-axis, and the rotation angle have been varied automatically

in order to detect the configuration that maximizes the net energy. All scenarios consider a doublet operational scheme with the parameters specified in Table 6.

In this section, computational results in the optimal geometrical configurations are analyzed with respect to the resulting velocity, pressure, and temperature fields, with the latter shown at the end of the lifetime as specified in Subsection 4.1.2.

Scenario LC Figures 15 and 16 show the velocity and pressure fields, as well as the temperature distribution corresponding to the optimization step 37, which maximizes the net energy among the 40 optimization steps for the scenario LC (see Figure 14).

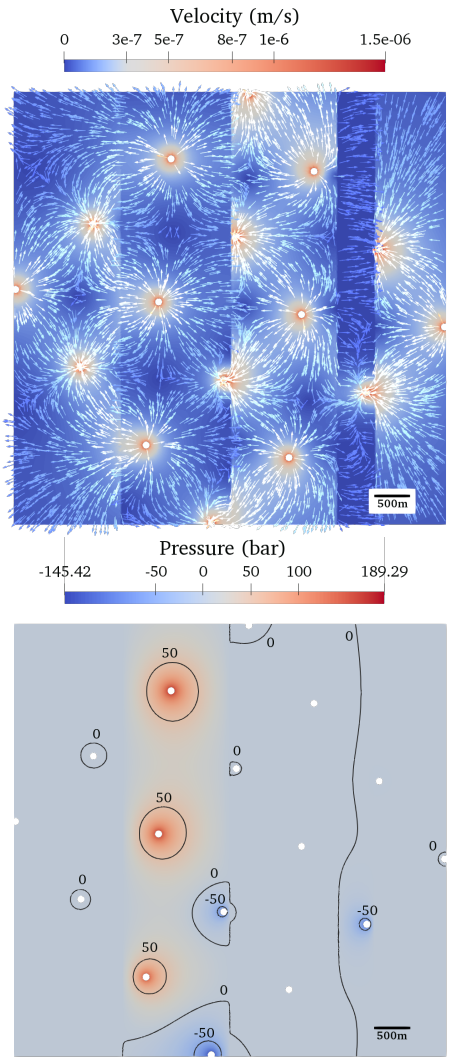

Figure 15: Setup LC in the optimal configuration (rotation angle $= 2.27\,\mathrm{rad}$, lattice size $= 1408\,\mathrm{m}$). Velocity filed with unscaled arrows (top) and pressure field with selected contours (bottom).

The corresponding optimal configuration is determined by a rotation angle $= 2.27\,\mathrm{rad}$ and lattice size $= 1408\,\mathrm{m}$ (translation is fixed to $0\,\mathrm{m}$). Figure 15 (top) shows that groundwater velocities are lowest in the zones of low permeability (dark blue stripes). According to the considered control variables, the optimal configuration is reached by accommodating the doublet lattice structure with a lattice size close to the maximum allowed, within an active modeling domain of $6 \times 6\,\mathrm{km}^2$. In terms of pressure, as shown in Figure 15 (bottom), the geothermal doublet lattice structure is rotated and the lattice size

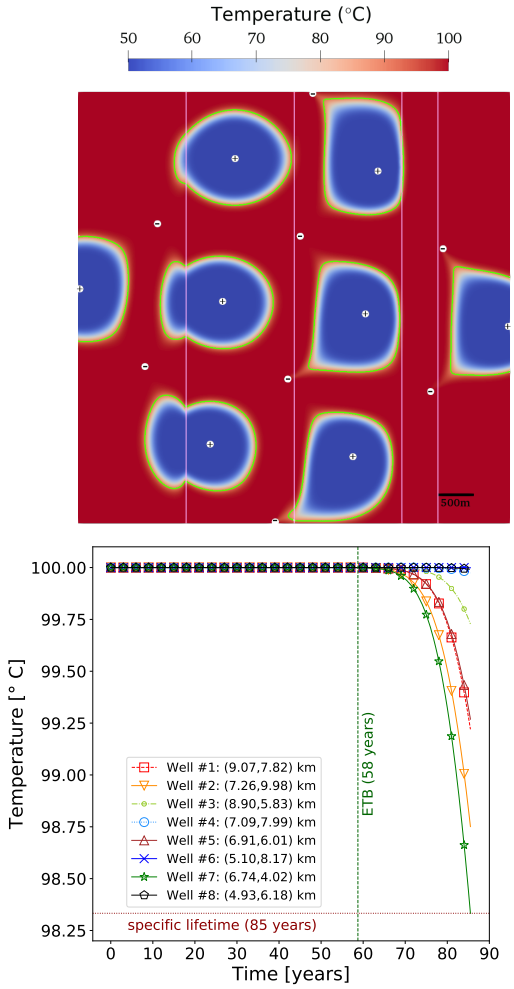

Figure 16: Setup LC in the optimal configuration (rotation angle $= 2.27\,\mathrm{rad}$, lattice size $= 1408\,\mathrm{m}$). Temperature field after 80 years of operation (top) with pink lines delimiting the different permeability regions and $90\,^{\circ}\mathrm{C}$ isolines depicted with a green line. Temperature evolution for each production well (bottom), showing the earliest thermal breakthrough (ETB). Note the different times of occurrence of the thermal breakthrough for each production well.

is adjusted, aiming at minimizing the pressure difference between injection and production wells, while striving for a well positioning that allows to maintain the aquifer temperature at the production wells as long as possible within the considered maximum time period of operation. This is manifested in Figures 15 and 16 by placing less than half (only six) of the wells inside the low permeability zones.

Maximizing the net energy implies minimizing the pressure difference between injectors and producers and maximizing the specific lifetime, which implies choosing the largest lattice size. As long as the thermal breakthrough does not occur within 80 years of operation (defined as the maximum operation time of the geothermal plant in this study), then the placement of the wells in a heterogeneous permeability field is controlled solely by the pressure difference between injectors and producers. As soon as the thermal breakthrough occurs, as illustrated in Figure 16, two competing mechanisms of minimizing the pressure difference between injection and production wells and maximizing the specific lifetime determine the maximum net energy.

The thermal breakthrough occurs at different times at the production wells (see Figure 16, bottom). In an optimization process involving complex hydraulic interaction between the injectors and producers

in heterogeneous permeability structures, the wells shall be deployed in a way that temperature drops at the production wells occur at the latest possible and the speed of the temperature decline is as low as possible.

Scenario L1 When prescribing a linearly varying initial temperature distribution as described in Subsection 8.3, similar simulation results as for the scenario LC are obtained. The maximum net energy in the case of L1 is obtained at the optimization step 38. However, due to the (on average) higher reservoir temperature, a higher value of the net energy is obtained for this scenario (see Figure 14). The optimal configuration is obtained with rotation angle $= 2.35\,\mathrm{rad}$ and lattice size $= 1397\,\mathrm{m}$ (translation is fixed to $0\,\mathrm{m}$). The flow and the pressure fields are depicted in Figure 17, while the temperature field after 80 years and the temperature evolution at the production wells are depicted in Figure 18.

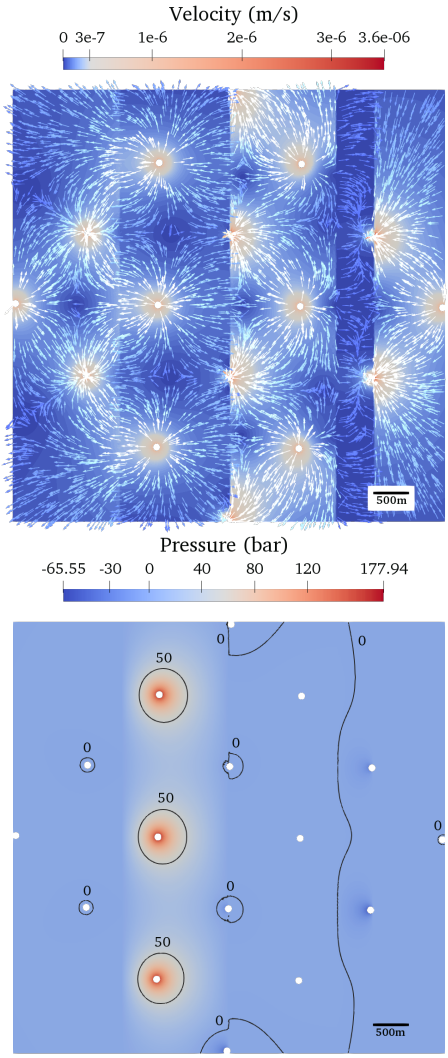

Figure 17: Setup L1 in the optimal configuration (rotation angle $= 2.35\,\mathrm{rad}$, lattice size $= 1397\,\mathrm{m}$). Velocity field with unscaled arrows (top) and pressure field with selected contours (bottom).

For the allowed degrees of freedom of movement of the well positions and the considered heterogeneous structure of the aquifer, the computed optimal configuration suggests that a moderately linearly varying reservoir temperature in the order of magnitude as described in Section 8.3 has almost no impact on the optimization. In contrast, variations in the permeability of several orders of magnitudes

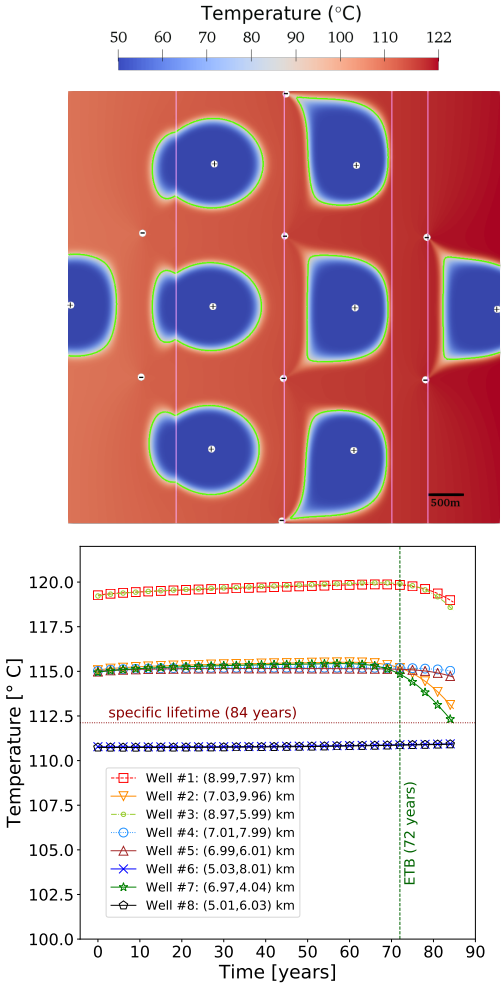

Figure 18: Setup L1 in the optimal configuration (rotation angle $= 2.35\,\mathrm{rad}$, lattice size $= 1397\,\mathrm{m}$). Temperature distribution after 80 years of operation (top) with pink lines delimiting the different permeability regions and $90\,^{\circ}\mathrm{C}$ isolines depicted with a green line. Temperature evolution or each production well (bottom), showing the earliest thermal breakthrough (ETB). Note that the production temperature for the wells placed in the colder parts, instead of dropping, is initially increasing over time, due to the fluid coming from hotter sections of the reservoir.

as it is typical for carbonate reservoirs have a greater impact on the optimal placement of the wells in such doublet arrangements for a utilization time of 80 years.

As can be seen in Figure 18 (bottom), the thermal breakthrough for the wells placed in the colder domains does not occur during the 80 years of simulation time. The majority of the production wells are deployed in a zone of intermediate temperature and just few of them are situated in the zone of higher temperatures.

We observe for the two setups LC and L1 that the lattice size is almost maximized with respect to the allowed range ($[500, 1414]\,\mathrm{m}$). The heterogeneous permeability structure yields a reduced velocity in the low permeability regions, which decelerate the thermal breakthrough in one direction while accelerating it in another direction. Within the geometrical constraints imposed, three injection wells are placed entirely in the lower permeability regions, yielding to high pressures in order to realize the demanded flow rates. Translation of the lattice, which is not allowed in these two cases, or further enlarging the lattice beyond the chosen control range would allow to place less wells in the low permeability regions. As can be seen in the velocity field displayed in Figure 17 (top), the maximum velocity reached for this scenario is around a factor 2.4 higher compared to the scenario LC (see Figure 15, top) due the placement of some wells directly at the boundary of the permeability contrast leading to steeper pressure gradients in the immediate vicinity of the well.

Another important observation relates to the impact that the number of injection wells surrounding a production well has on the time of occurrence of the thermal breakthrough. We observe that the production wells located north and south in the scenarios LC and L1 are surrounded by the least number of injectors and undergo the earliest occurrence of the thermal breakthrough for the simulation time considered (see Figures 16 and 18). In a regular lattice structure of doublet arrays, production wells located in the interior are surrounded by four injectors, whereas production wells located at the edges are surrounded by three or two injectors. Hence, an interior injection well distributes its induced flow rate to four surrounding production wells in different directions. That way the velocity of the fluid along each direct line connecting injection and production wells is lower than in the case of fewer surrounding production wells. Consequently, the progression of the cooling front emanating from the injection wells surrounded by the largest number of producers is slowed down, which is even promoted by unfavorable permeability structures. The hydraulic interaction between injectors and producers in combination with a heterogeneous permeability distribution explains the observation that those production wells, which fulfill both conditions, experience the earliest thermal breakthrough.

Scenario L2 The setup L2 allows for the rigid translation and rotation of the lattice structure. This scenario is intended to examine the impact that a moderately linearly varying reservoir temperature has on the optimal placement of a rigid lattice arrangement of doublet arrays. To that end, a homogeneous permeability structure is considered.

The optimal configuration corresponds to the rotation angle $= 2.97\,\mathrm{rad}$ and the horizontal translation $= 1206\,\mathrm{m}$ (lattice size is fixed to $600\,\mathrm{m}$). Figures 19 and 20 visualize the velocity and pressure fields, as well as the temperature distribution at a specific lifetime of 24 years and the temperature evolution for each production well. We observe a significant translation towards higher reservoir temperatures.

In contrast to the simulation results concerning the previous setups LC and L1, the pressure range of values is much lower for the setup L2 due to the higher average permeability that characterizes this setup. As can be also seen in Figure 20 (bottom), the specific lifetime for the setup L2 is much shorter than those computed for the previous setups LC and L1, since the lattice size (inter-well distance) is much smaller and the higher average permeability is more favorable for an earlier occurrence of the

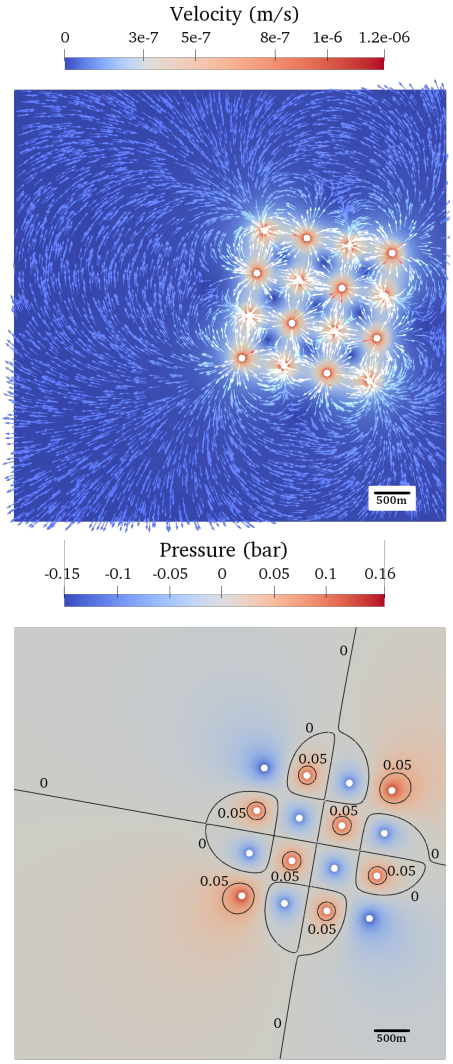

Figure 19: Setup L2 in the optimal configuration (rotation angle $= 2.97\,\mathrm{rad}$, translation $= 1206\,\mathrm{m}$). Velocity field with unscaled arrows (top) and pressure field with selected contours (bottom).

thermal breakthrough in the setup L2. Since the resulting pressure field remains constant over the entire simulation time, only the temperature distribution in reservoir drives the search for the optimal placement of the doublet lattice arrangement. Finding the optimal configuration in this case, where the net energy is maximized, implies maximizing the temperature difference between injectors and producers in a linearly varying temperature field. As long as the thermal breakthrough is not established, the maximum net energy of the system of doublets is solely controlled by the initial temperature difference of the respective doublets. Once the thermal breakthrough is established at different geothermal doublets, the mixed fluid temperature of the respective cooling fronts at the production wells and consequently the different speeds of temperature declines control the maximum net energy of the system (see Figure 20, bottom).

Scenario L3 In the scenario L3, which differs from the previous scenario L2 only in that the permeability distribution is heterogeneous, the optimal configuration corresponds to the rotation angle $= 1.53\,\mathrm{rad}$ and the translation $= -70.35\,\mathrm{m}$ (lattice size is fixed to $600\,\mathrm{m}$). The simulation results for this case are visualized in Figures 21 and 22.

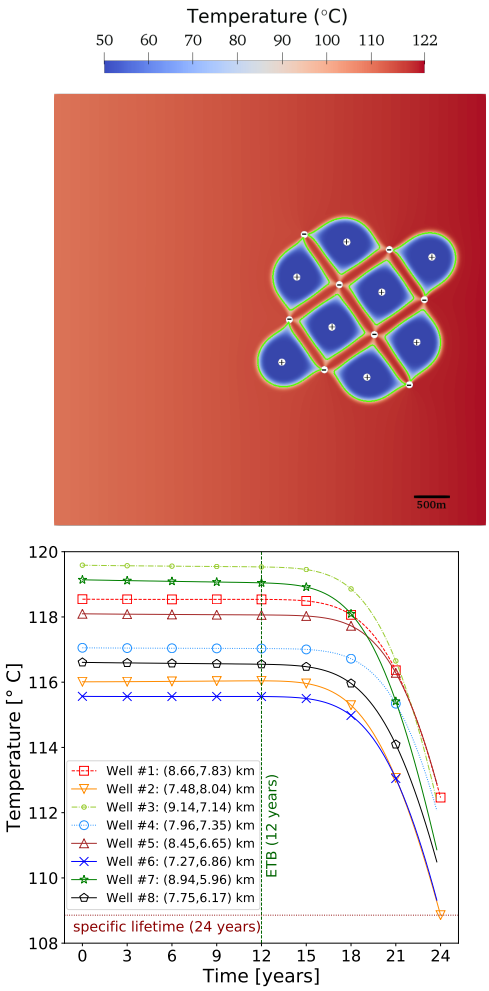

Figure 20: Setup L2 in the optimal configuration (rotation angle $= 2.97\,\mathrm{rad}$, translation $= 1206\,\mathrm{m}$). Temperature field at the specific lifetime of 24 years (top) with pink lines delimiting the different permeability regions and $90\,^{\circ}\mathrm{C}$ isolines depicted with a green line. Temperature evolution for each production well (bottom), showing the earliest thermal breakthrough (ETB). Note the different speeds of temperature drop for the respective production wells.

As can be seen in the velocity and pressure fields illustrated in Figure 21, for the considered reservoir temperature variation, the optimal placement of the rigid lattice of doublets is mainly controlled by the permeability structure. For a fixed lattice size equal to $600\,\mathrm{m}$ and the considered degrees of freedom of movement (translation and rotation), the optimal configuration is reached by placing one half of the lattice structure in a low permeability zone and the other half in a high permeability zone, where the latter has a higher average temperature. On the one hand, combining lower permeabilities with lower production temperatures for half of the production wells allows to prolong the time of maximum production temperature at the expense of higher pressure. On the other hand, installing the other half in a higher permeability region with a higher average production temperature necessitates lower pressures at the price of an earlier thermal breakthrough (see Figures 21-22). The permeability contrast between the lattice halves acts as a hydraulic barrier resulting in a deceleration of the cooling fronts evolution across the permeability contrast towards the zone of lower permeability.

The lateral temperature gradient in the order of magnitude considered in this study seems to have no significant impact on the translation of the lattice in the presence of the heterogeneous permeability structure with contrasts of several orders of magnitude.

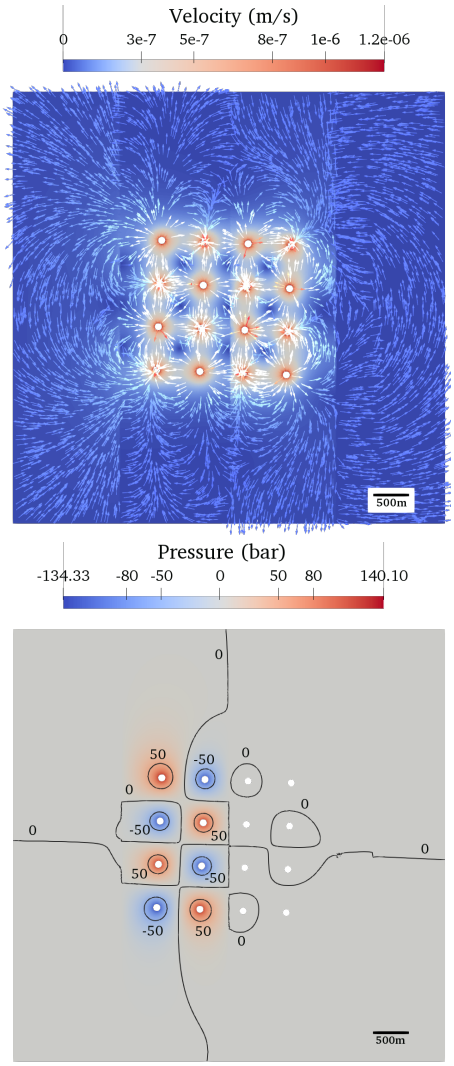

Figure 21: Setup L3 in the optimal configuration (rotation angle $= 1.53\,\mathrm{rad}$, translation $= -70.35\,\mathrm{m}$). Velocity field with unscaled arrows (top) and pressure field with selected contours (bottom). Note in the pressure field (bottom) that half of the wells are situated outside the low permeability zones.

The fixed lattice size in the scenarios L2 and L3 yields a much smaller specific lifetime of 24 and 22.75 years, respectively. This is due to the fixed lattice size equal to $600\,\mathrm{m}$ and it is in line with the net energy results (see Figure 14). In the previous scenarios LC and L1, the lattice size was allowed to vary and reached almost maximum permissible values, resulting in a much longer lifetime. This suggests that the inter-well distance predominantly controls the occurrence time of the thermal breakthrough and hence the economic lifetime of doublet geothermal facilities for the considered conditions.

From a more general point of view, the simulation results indicate that the pressure differences between injectors and producers generated by the combination of the flow rates imposed as exploitation strategy and the permeability structure have a stronger (negative) impact on the net energy compared to the temperature differences between injectors (fixed value) and producers generated by the considered lateral thermal gradient in reservoir.

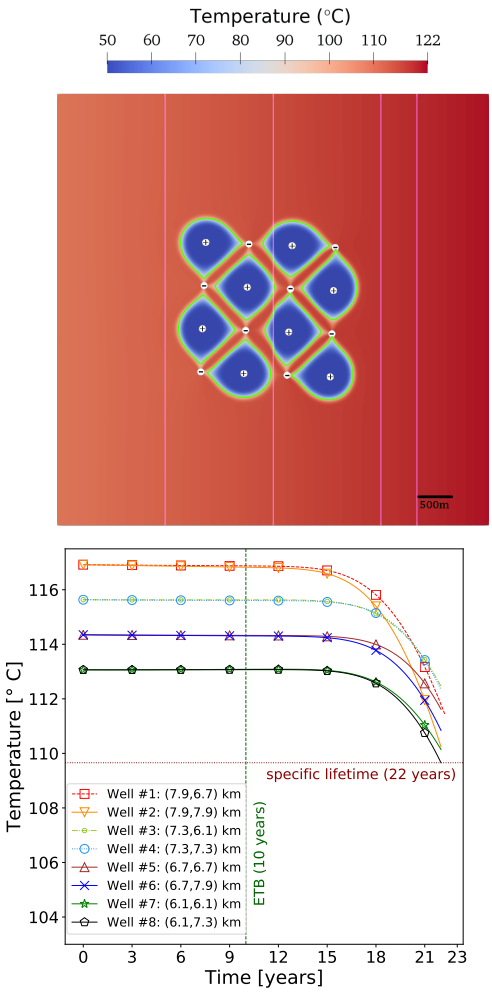

Figure 22: Setup L3 in the optimal configuration (rotation angle $= 1.53\,\mathrm{rad}$, translation $= -70.35\,\mathrm{m}$). Temperature field at the specific lifetime of 22.75 years (top) with pink lines delimiting the different permeability regions and $90\,^{\circ}\mathrm{C}$ isolines depicted with a green line. Temperature evolution for each production well (bottom), showing the earliest thermal breakthrough (ETB). Note the different speeds of temperature drop of the respective production wells.

9.3 Hexagon configurations

In this section we present simulation results for five different scenarios in the case of a geothermal hexagonal multi-well structure (see Section 8.1.2 and Table 4). In all cases, initial and boundary aquifer temperature are set to a constant value. Essentially, different operational strategies in a fault-controlled geothermal reservoir with varying damage zone width are examined in order to understand the impact that operational, hexagon geometrical parameters, and reservoir permeability structures have on the optimal configuration concerning the maximum net energy.

For all scenarios, we monitor the optimization activity via visualizing the net energy, the hexagon radius, and the hexagon rotation angle against the optimization step. For the scenarios tested with varying damage zone width (setups $\mathrm{H}_{(3,3)}$, $\mathrm{H}_{(4,2)}$, and $\mathrm{H}_{(2,4)}1$), only the results corresponding to the final/optimal positioning for a width of $400\,\mathrm{m}$ are presented. In terms of maximum net energy, this damage zone width is the most promising considered scenario. This is due to the fact that a larger sub-region of the modeling domain has a higher permeability, which allows to place two wells partly inside the fault damage zone, such that on the one hand the pressure difference is smaller and on the

other hand the progress of the cooling front is slower.

It is important to note that, except for the scenario $H_{(2,4)}2$, where the fault damage zone centrally passes through the center of the hexagon, the optimization is not able to place two wells entirely inside the damage zone. Further, for decreasing damage zone width, the damage zone moves away from the center of the hexagon.

9.3.1 $H_{(3,3)}$ – 3 injection and 3 production wells

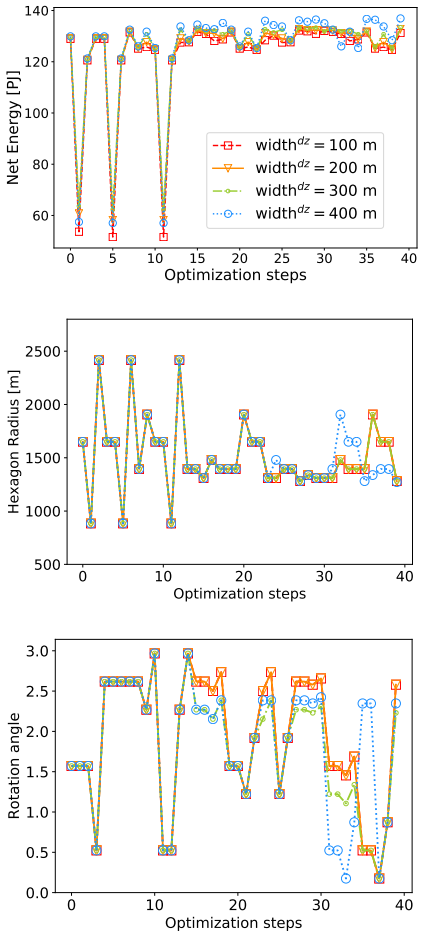

Figure 23: Setup $H_{(3,3)}$ – Net energy (top), hexagon radius (middle), hexagon rotation angle (bottom) over 40 optimization steps with the global optimization algorithm DIRECTL for different damage zone widths.

During the first optimization steps, we observe a strong variation of almost a factor 3 in the resulting net energy, see Figure 23. The smallest values of the net energy correspond to small hexagon radii of less than $1\,\mathrm{km}$. Hence, in this case the inter-well distance has a much stronger impact on the net energy than the rotation angle, which is for all damage zone widths strongly varying until the end of the 40 optimization steps. For the hexagon radius, we observe structural repetitions, although the corresponding angles are changed. This may be related to the fact that for similar hexagon radii, different rotation angles of the hexagonal multi-well arrangement of alternated injectors and producers deliver similar values of net energy.

The final and optimal positioning is basically the same for the different damage zone widths, however,

the largest considered damage zone of $400\,\mathrm{m}$ width yields the maximal net energy, which decreases with decreasing damage zone width.

Figures 24–25 illustrate the simulation results in terms of the velocity, pressure, and temperature fields for the optimal configuration.

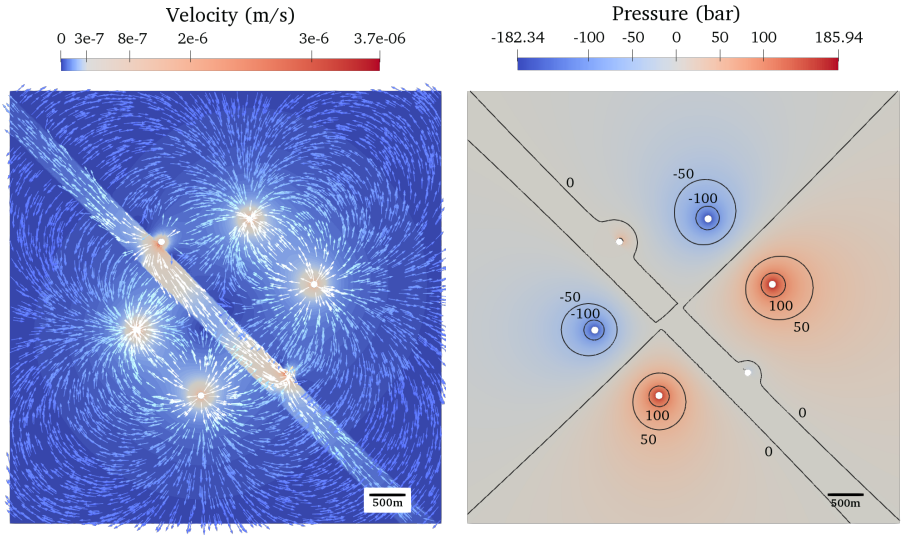

Figure 24: Setup $\mathrm{H}_{(3,3)}$ in the optimal configuration (rotation angle $= 2.35\,\mathrm{rad}$, hexagon radius $= 1271\,\mathrm{m}$). Velocity field with unscaled arrows (top) and pressure field with selected contours (bottom) for a fault damage zone width of $400\,\mathrm{m}$.

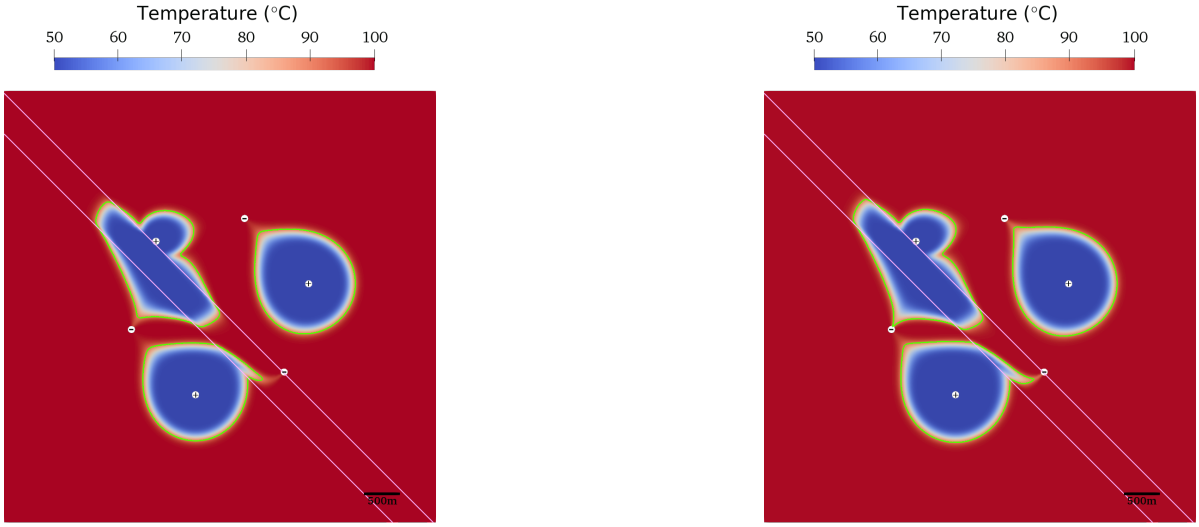

Figure 25: Setup $\mathrm{H}_{(3,3)}$ in the optimal configuration (rotation angle $= 2.35\,\mathrm{rad}$, hexagon radius $= 1271\,\mathrm{m}$). Temperature distribution after 80 years of operation (top) and at the end of the specific lifetime after 86.75 years of operation (bottom). A $90°$C isoline is depicted with a green line. The pink lines delimit the different permeability regions.

The optimal placement of the wells is reached by deploying one injector and one producer in or as close as possible to the fault damage zone (at the border of the damage zone), which is a zone of enhanced permeability. This way the pressure difference between one injection and one production well is minimized, while the inter-well distance of this doublet is largest. In addition, the progress of the corresponding cooling front is channeled in the direction of the main axis of the fault damage zone and

decelerated in the direction of the other neighboring production wells (see Figure 25). That way the time of occurrence of the thermal breakthrough is substantially delayed and thus the specific lifetime prolonged (Figure 26).

The specific lifetime for the final/optimal positioning of the wells occurs shortly after 80 years of operation. Another important observation relates to the thermo-hydraulic behavior of the two wells (doublet) placed at the farthest distance from the damage zone. The pressure and temperature fields of that doublet are not significantly influenced by the other wells such that the typical tear drop shape of the cooling front can be observed – similar to a single doublet simulation (see Figure 12). Further, the temperature drops much faster at the production well situated at the westernmost corner of the multi-well hexagon than the other two production wells for the simulation time considered. As can be seen in the velocity field, in the vicinity of the wells partly inside the fault damage zone we observe a predominantly linear flow behavior, whereas a bilinear flow is exhibited away from the wells at the extremes of the damage zone and matrix.

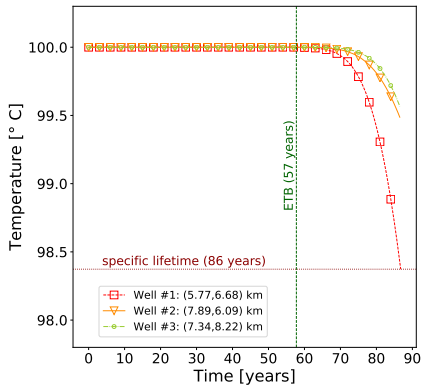

Figure 26: Setup $H_{(3,3)}$ in the optimal configuration (rotation angle $= 2.35\,\mathrm{rad}$, hexagon radius $= 1271\,\mathrm{m}$). Temperature evolution for each production well showing the earliest thermal breakthrough (ETB).

9.3.2 Setup $H_{(4,2)}$ – 4 injection and 2 production wells

Figure 27 compares the optimization processes for different widths of the fault damage zone. Similar as for the setup $H_{(3,3)}$, the damage zone width of $400\,\mathrm{m}$ yields the largest net energy. We also recognize a strong influence of the hexagon radius on the resulting net energy.

The resulting velocity and pressure fields for the optimal placement of the multi-well hexagonal configuration are displayed in Figure 28.

In this setup, each production well has a twice as high flow rate as any injection well. The optimal configuration has been reached by placing the production wells as close as possible to the fault damage zone (around the border). As shown in Figure 28 (top), the velocity field shows three different flow types (linear, bilinear, and radial) in the proximity of the wells in the fault damage zone and the matrix. In the vicinity of wells outside the fault damage zone, a radial flow behavior is observed. In the neighborhood of the production wells a linear flow is established in the damage zone, whereas towards the center of the fault damage zone the flow gradually transforms into bilinear flow.

The placement of the wells with higher flow rates in or near the zone of higher permeability allows the pressure to diffuse with least resistance so that the pressure difference between injectors and

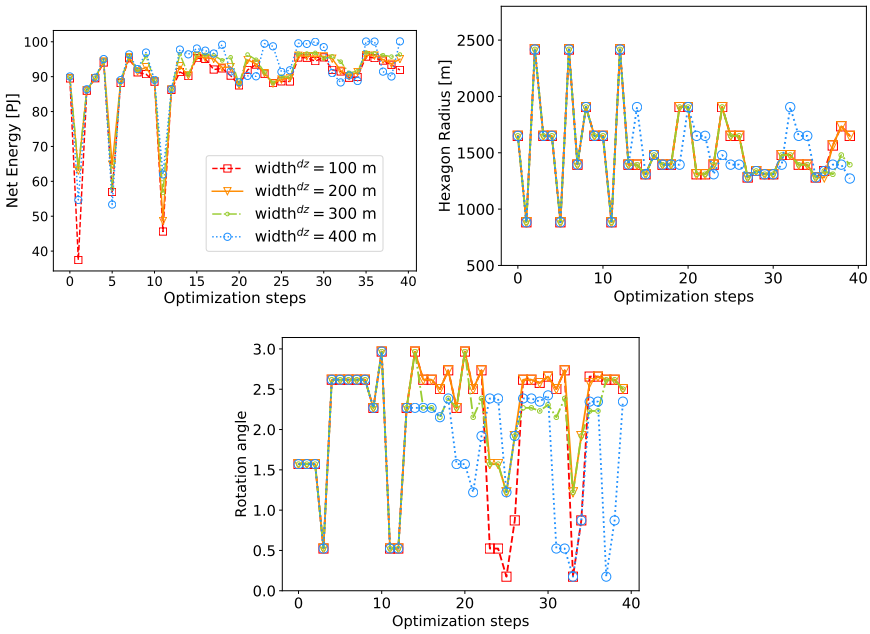

Figure 27: Setup $H_{(4,2)}$ – Net energy (top), hexagon radius (middle), and hexagon rotation angle (bottom) for 40 optimization steps with the global optimization algorithm DIRECTL for different damage zone widths.

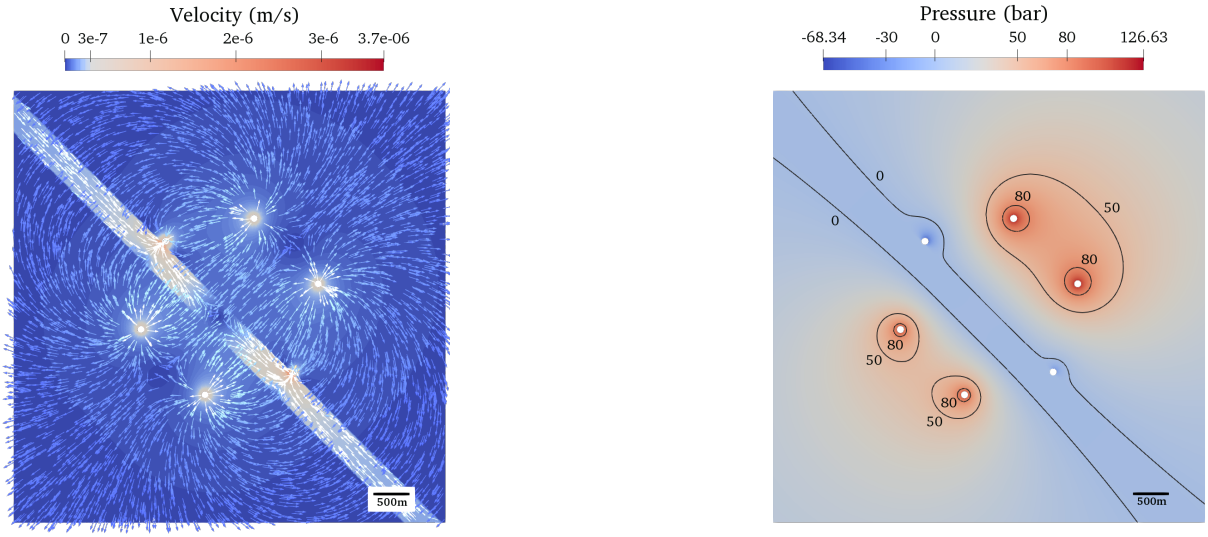

Figure 28: Setup $H_{(4,2)}$ in the optimal configuration (rotation angle $= 2.35\,\mathrm{rad}$, hexagon radius $= 1271\,\mathrm{m}$). Velocity field with unscaled arrows (top) and pressure field with selected contours (bottom) for a damage zone width of $400\,\mathrm{m}$.

producers is as low as possible. The temperature distribution after 80 years and at the end of the specific lifetime of 133.55 years of operation are shown in Figure 29.

Also the temperature fields reveal that placing the production wells as near as possible to the fault damage zone contributes to the deceleration of the cooling front from the injectors towards the producers. The cooling fronts develop essentially circular with a slight tendency towards the fault damage zone and reach the production wells almost simultaneously after 81 years (thermal breakthrough), by passing along and through the high permeability region. The fact that the highest net energy is

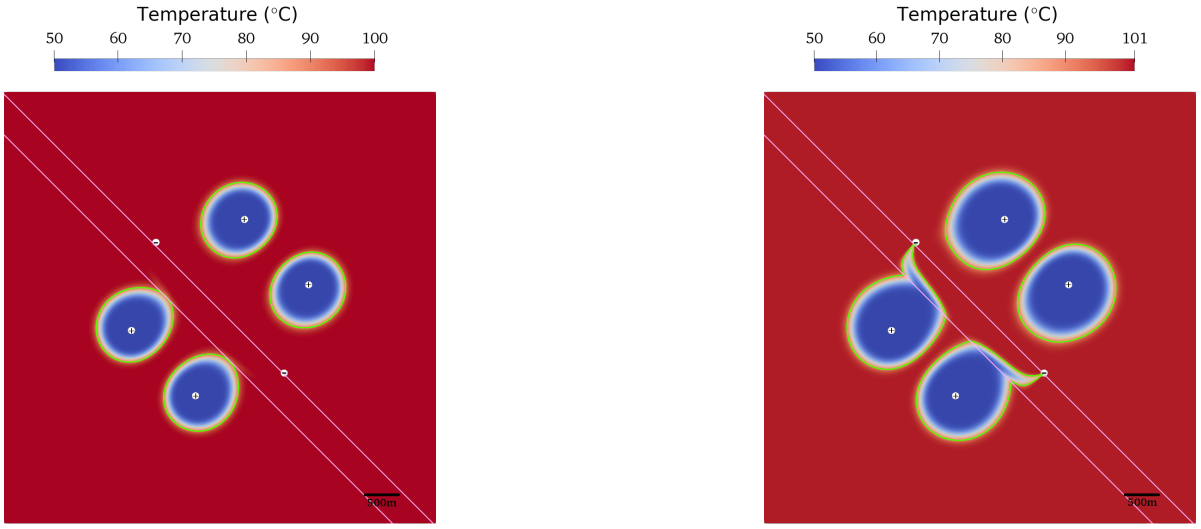

Figure 29: Setup $H_{(4,2)}$ in the optimal configuration (rotation angle $= 2.35\,\mathrm{rad}$, hexagon radius $= 1271\,\mathrm{m}$). Temperature distribution after 80 years of production (top) and at the end of the specific lifetime after 133.55 years of operation (bottom). Damage zone width equal to $400\,\mathrm{m}$. A $90\,^{\circ}\mathrm{C}$ isoline is depicted with a green line. The pink lines delimit the different permeability regions.

reached with the largest damage zone width reveals that although different competing mechanisms at different stages of the thermo-hydraulic interaction between the wells are involved, placing the wells with highest flow rates as near as possible to the high permeable zone is decisive for the optimization of the net energy for the considered conditions.

The temperature evolution for the two production wells and the optimal positioning is displayed in Figure 30. It reveals a symmetric character with respect to the fault damage zone, with a similar occurrence time of the thermal breakthroughs and speed of temperature decline for both production wells.

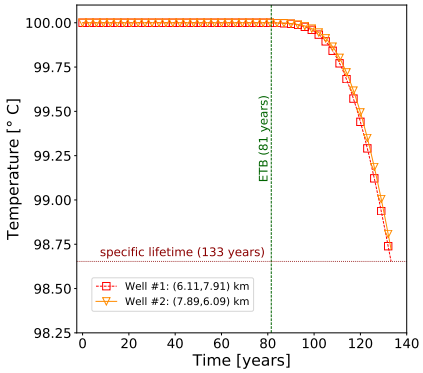

Figure 30: Setup $H_{(4,2)}$ in the optimal configuration (rotation angle $= 2.35\,\mathrm{rad}$, hexagon radius $= 1271\,\mathrm{m}$). Temperature evolution at the production wells until the specific lifetime is reached, showing the earliest thermal breakthrough (ETB).

9.3.3 Setups $H_{(2,4)}1$ and $H_{(2,4)}2$ – 2 injection and 4 production wells

This section presents the simulation results of two multi-well hexagonal scenarios: (i) an asymmetric hexagon with respect to the main axis of the fault damage zone with varying damage zone width and

(ii) a symmetric hexagon with respect to the main axis of the fault damage zone with fixed damage zone width equal to $400\,\mathrm{m}$, such that the optimization procedure is able to place wells entirely inside the damage zone.

As in the Section 9.3.2, the hexagon radius primary controls the optimization of the net energy, see Figure 31. In particular, we see that the case with centered damage zone yields a net energy value (at the 36th optimization step) higher than any of the other considered cases.

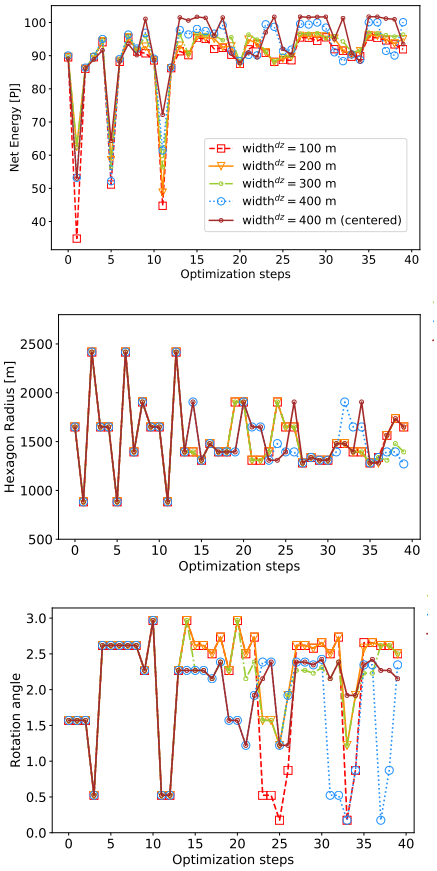

Figure 31: Setup $\mathrm{H}_{(2,4)}1$ and $\mathrm{H}_{(2,4)}2$ – Net energy (top), hexagon radius (middle), and rotational angle (bottom) computed in each of the 40 optimization steps with the global optimization algorithm DIRECTL for different damage zone widths and hexagon center positions.

Figures 32–34 show the resulting velocity, pressure, and temperature fields, as well as the temperature evolution at the production wells for the setup $\mathrm{H}_{(2,4)}1$ in the optimal configuration with damage zone width $400\,\mathrm{m}$.

As in the case $\mathrm{H}_{(4,2)}$, two wells are located as near as possible to the damage zone. This time, however, the two injection wells have a twice higher flow rate (compared to the production wells) and are deployed as close as possible to the high permeability zone, which allows to reduce the pressure difference between injectors and producers the most.

The cold water plumes (of $90\,^{\circ}\mathrm{C}$ or less), shown in Figure 33, evolve along the high permeability channel, but stay separated from each other during the considered time range (118.75 years). The cold water fronts leave the damage zone towards the production wells on the other side of the damage zone. After 77 years the initial thermal breakthrough happens and the specific lifetime of the multi-well system is essentially controlled by two doublets. The two production wells located at the same side as the injection wells with respect to the damage zone have a notably limited influence on the cold water

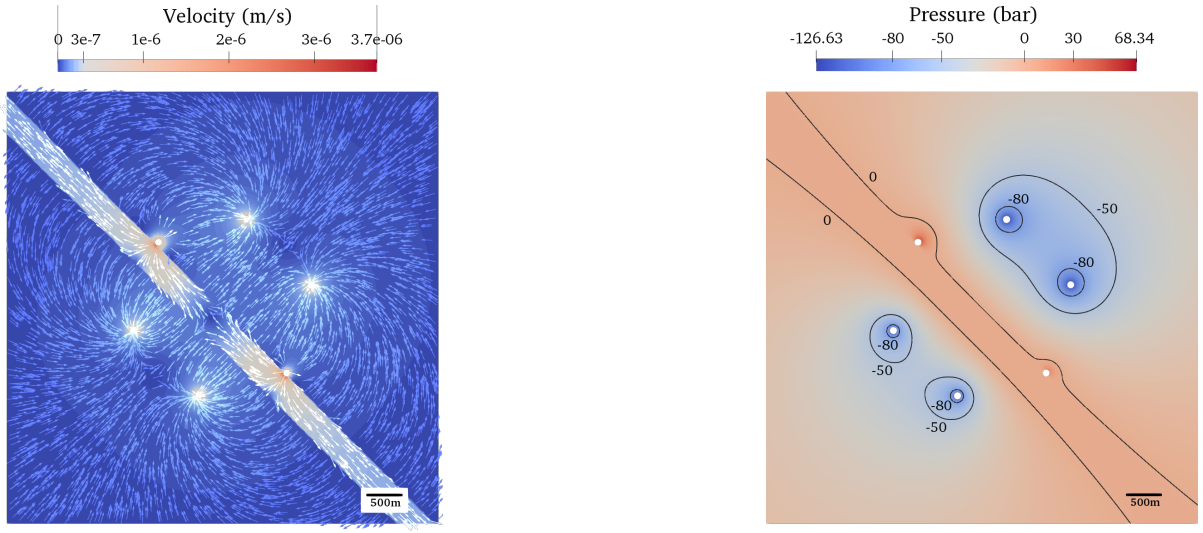

Figure 32: Setup $H_{(2,4)}1$ in the optimal configuration (rotation angle $= 2.35\,\mathrm{rad}$, hexagon radius $= 1271\,\mathrm{m}$). Velocity field with unscaled arrows (top) and pressure field with selected contours (bottom) for the damage zone width $400\,\mathrm{m}$.

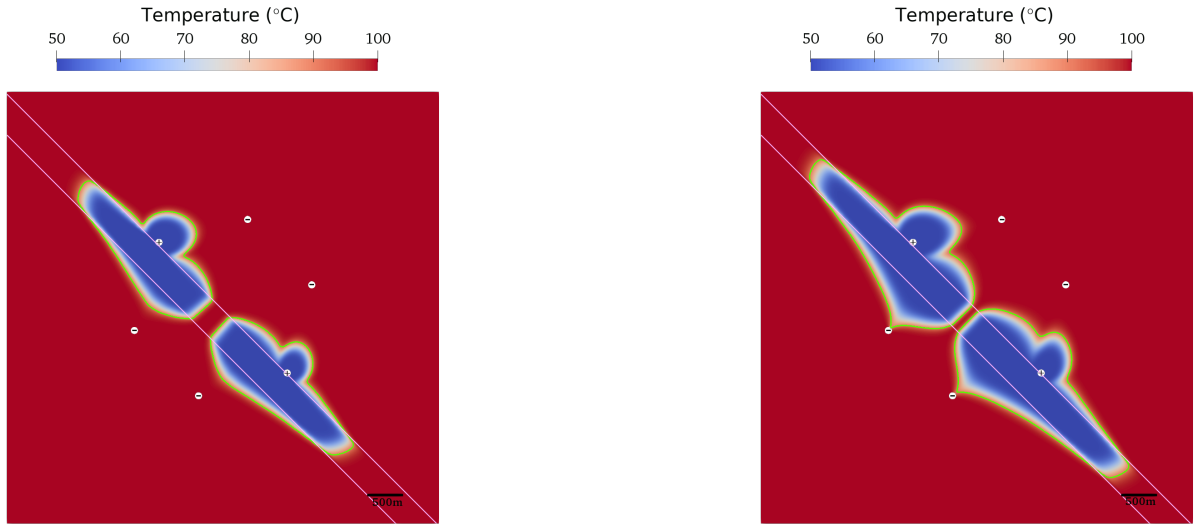

Figure 33: Setup $H_{(2,4)}1$ in the optimal configuration (rotation angle $= 2.35\,\mathrm{rad}$, hexagon radius $= 1271\,\mathrm{m}$). Temperature distribution after 80 years of operation (top) and at the end of the specific lifetime after 118.5 years of operation (bottom). A $90\,^{\circ}\mathrm{C}$ isoline is depicted with a green line. The pink lines delimit the damage zone.

plume. This can also be seen in the temperature evolution for each production well (Figure 34).

Placing the injection wells with higher flow rates in or as close as possible to the high permeability zone channels the cooling front along the fault damage zone and decelerates the progress of the cooling front in the direct line connecting injectors and producers. The velocity field illustrates different flow patterns. It is predominantly linear in some parts of the fault damage zone and of bilinear type in others, where fluid flows from the damage zone into the matrix.

In the scenario $H_{(2,4)}2$, the center of the hexagon multi-well structure is situated on the main axis of a fault damage zone of $400\,\mathrm{m}$ width. In this case, it is geometrically allowed for the optimization procedure to place two wells entirely inside the damage zone.

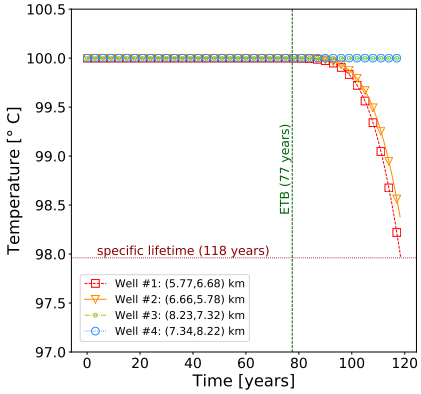

Figure 34: Setup H$_{(2,4)}1$ in the optimal configuration (rotation angle $= 2.35\,\mathrm{rad}$, hexagon radius $= 1271\,\mathrm{m}$). Temperature evolution for each production well until the end of the specific lifetime.

As can be seen in the resulting velocity, pressure, and temperature fields in Figures 35, 36, 37, and 38 in the optimal configuration (optimization step 36), the two injection wells are placed entirely inside the damage zone.

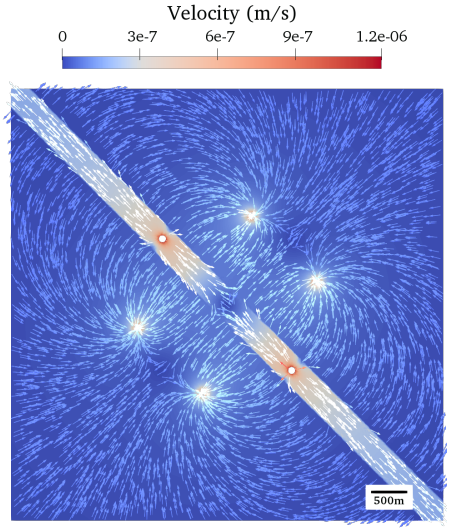

Figure 35: Setup H$_{(2,4)}2$ in the optimal configuration (rotation angle $= 2.35\,\mathrm{rad}$, hexagon radius $= 1281\,\mathrm{m}$). Velocity field with unscaled arrows.

This arrangement results in relatively small pressures for these injection wells, although their flow rate is twice as large as for the four production wells. The velocity, pressure, and temperature patterns obtained for this symmetric case (with respect to the fault damage zone main axis) display a configuration of two geothermal triplets behaving similarly. Analogous to the previous scenario H$_{(2,4)}1$, the cooling front is channeled in the high permeability zone, decelerating it in the direction to the neighboring producers. This way the earliest thermal breakthrough time and the specific lifetime are significantly delayed. After around 80 years simulation time, the cold water front starts to depart from the damage zone towards the production wells, forming two triplets as mentioned previously. At the end of the specific lifetime of 171 years, the two cold water plumes have already partially connected with each other, see Figure 39.

In comparison to the previous scenario H$_{(2,4)}1$, the specific lifetime is around 50 years longer. It is worth mentioning that since the the two wells in the damage zone are not exactly located on the central

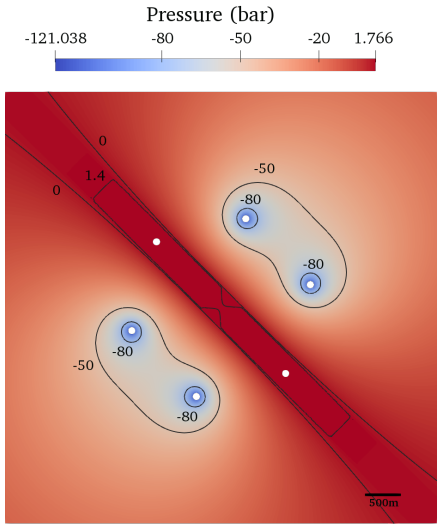

Figure 36: Setup $\mathrm{H}_{(2,4)}2$ in the optimal configuration (rotation angle $= 2.35\,\mathrm{rad}$, hexagon radius $= 1281\,\mathrm{m}$). Pressure field with selected contours.

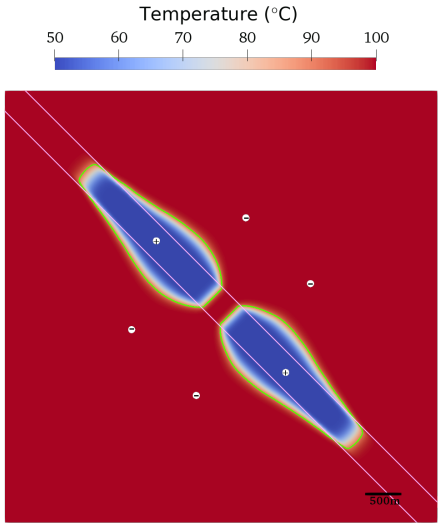

Figure 37: Setup $\mathrm{H}_{(2,4)}2$ in the optimal configuration (rotation angle $= 2.35\,\mathrm{rad}$, hexagon radius $= 1281\,\mathrm{m}$). Temperature distribution after 80 years of production. A $90\,^{\circ}\mathrm{C}$ isoline is depicted with a green line. The pink lines delimit the damage zone.

axis of the fault damage zone, a slightly asymmetric evolution of the cooling front is established. This explains why the temperature decline for two producers slightly differs from the other two pairs, see Figure 39.

9.3.4 Setup $\mathrm{H}_{(2,4)}3$ – 2 injection and 4 production wells

The setup $\mathrm{H}_{(2,4)}3$ considers a hexagon multi-well arrangement in a reservoir crossed by a fault damage zone with a relatively low healing capacity. The damage zone width is set to $200\,\mathrm{m}$ and the center of the hexagon does not coincide with the main axis of the fault damage zone. To better illustrate the simulation results, this setup is compared to the case of a hexagonal multi-well arrangement embedded in a reservoir with a homogeneous permeability distribution ($K = 3 \cdot 10^{-11}\,\mathrm{m}^2$). Figure 40

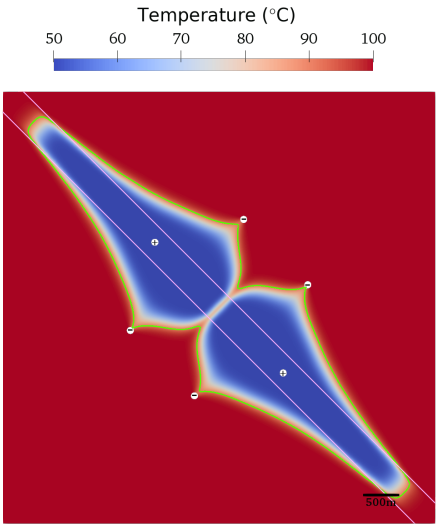

Figure 38: Setup $\mathrm{H}_{(2,4)}2$ in the optimal configuration (rotation angle $= 2.35\,\mathrm{rad}$, hexagon radius $= 1281\,\mathrm{m}$). Temperature distribution after at the end of the specific lifetime of 171 years.. A $90\,^{\circ}\mathrm{C}$ isoline is depicted with a green line. The pink lines delimit the damage zone.

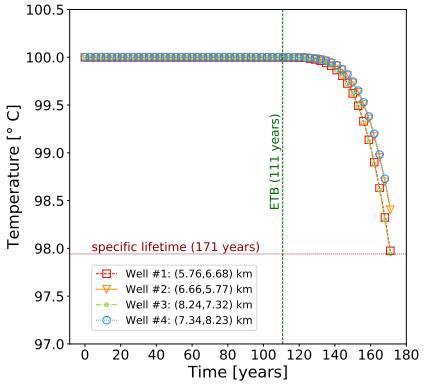

Figure 39: Setup $\mathrm{H}_{(2,4)}2$ in the optimal configuration (rotation angle $= 2.35\,\mathrm{rad}$, hexagon radius $= 1281\,\mathrm{m}$). Temperature evolution for each production well for the damage zone width $400\,\mathrm{m}$ passing through the center of the hexagon.

contrasts the optimization results for these two cases.

During the 40 optimization steps, the net energy behaves for both scenarios very similar and after an initial oscillating behavior it becomes almost constant. We observe also for these scenarios that small radii yield small net energies (optimization steps 2, 6, and 12, see Figure 40). In the presence of a healed fault, this effect is even stronger due to reservoir compartmentalization. Notice that in this scenario the optimization excludes rotation angles of $\geqslant 1\,\mathrm{rad}$ and thus the option to place the injection wells inside the healed fault, which would lead to higher pressure differences between injectors and producers but would also delay the thermal breakthroughs.

Figures 41–42 exhibit the velocity, pressure, and temperature fields for the optimal configuration of the hexagonal arrangement.

The optimal configuration is reached by placing a triplet on each side of the weakly healed fault, resulting in similar patterns for the velocity, pressure, and cooling front evolution in both sides of the reservoir with respect to the fault. The spatio-temporal evolution of the cooling fronts is similar to

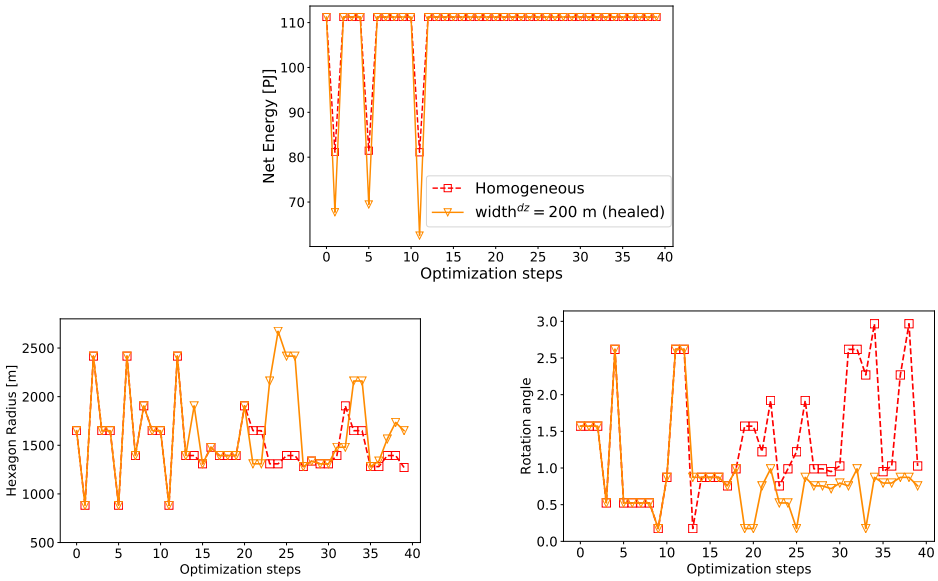

Figure 40: Setup $\mathrm{H}_{(2,4)}3$ *vs.* homogeneous reservoir – Net energy, hexagon radius, and hexagon rotation angle during 40 optimization steps with the global optimization algorithm DIRECTL.

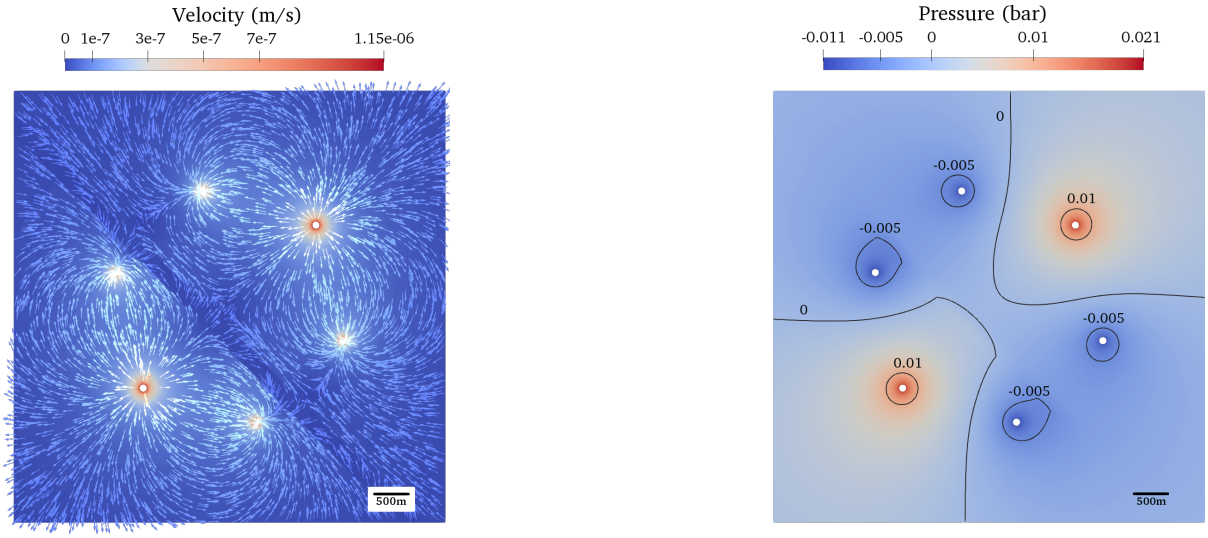

Figure 41: Setup $\mathrm{H}_{(2,4)}3$ in the optimal configuration (rotation angle $= 0.76\,\mathrm{rad}$, hexagon radius $= 1650\,\mathrm{m}$). Velocity field with unscaled arrows (top) and pressure field with selected contours (bottom) for the healed damage zone of width $200\,\mathrm{m}$.

the case of the reservoir with homogeneous permeability. It is worth mentioning that the permeability contrast between the damage zone of $200\,\mathrm{m}$ width and the matrix is only one order of magnitude. Thus, a slight compartmentalization into two equally homogeneous reservoir sectors occurs.

Due to the initial geometrical configuration, one triplet is placed closer to the healed damage zone than the other triplet and both are slightly rotated with respect to the main axis of the fault damage zone. This explains the different temperature declines observed at the respective production wells in Figure 43. The specific lifetime for this scenario is 205.75 years.

The geophysical plausibility of the simulation results in terms of the reached optimal deployment of geothermal multi-well systems in different reservoir structures and geothermal field development strategies corroborates the robustness of our proposed numerical framework.

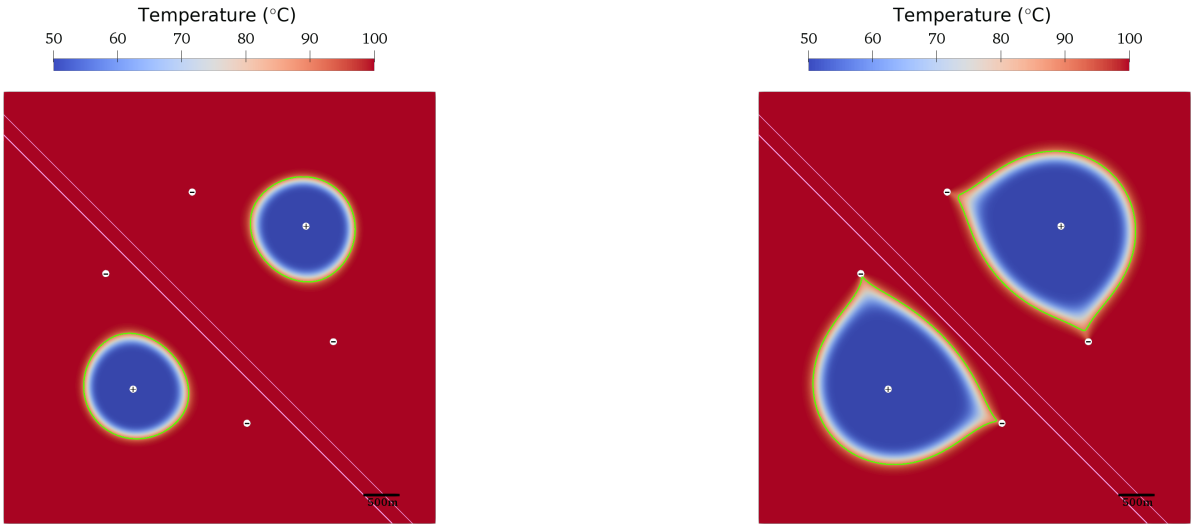

Figure 42: Setup $H_{(2,4)}3$ in the optimal configuration (rotation angle $= 0.76\,\mathrm{rad}$, hexagon radius $= 1650\,\mathrm{m}$). Temperature distribution after 80 years of operation (top) and at the end of the specific lifetime after 205.75 years of operation (bottom). A $90\,^{\circ}\mathrm{C}$ isoline is depicted with a green line. The pink lines delimit the healed damage zone.

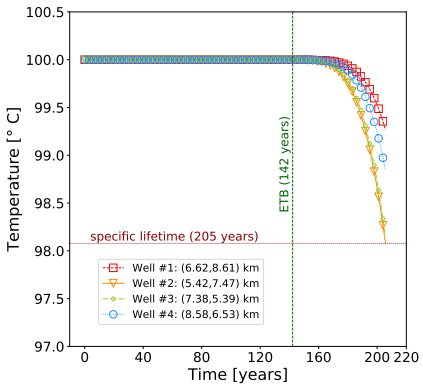

Figure 43: Setup $H_{(2,4)}3$ in the optimal configuration (rotation angle $= 0.76\,\mathrm{rad}$, hexagon radius $= 1650\,\mathrm{m}$). Temperature evolution for each production well for the healed damage zone of width $200\,\mathrm{m}$.

10 Conclusions

We propose a computational framework for the modeling and simulation of coupled thermo-hydraulic reservoir processes in hot sedimentary aquifers, focusing on the optimization of smart multi-well systems for district heating. Our approach is based on coupled finite element methods for a generalized Darcy–Brinkman flow and for the heat advection. Geothermal wells are introduced using an immersed boundary approach that does not require the exact discretization of the well boundary within the computational mesh. The combination of two open source solvers has been used to solve an optimization problem concerning geothermal energy production depending on the well position in heterogeneous reservoir conditions. In particular, we investigated the case of multi-well arrays in the form of a lattice and a hexagonal structure, considering structural- and facies-related heterogeneities as well as varying reservoir temperatures, typically encountered in the Upper Jurassic (Malm) aquifer in the Greater Munich region. We focused on confined aquifers and reduced to two-dimensional domains. The exten-

sion to three dimensions requires a generalization of the non-matching immersed method for the wells, and will be tackled in upcoming work. Further aspects that will be object of future research include the utilization of gradient-based optimization methods and of model-order reduction techniques such as reduced basis or proper orthogonal decomposition methods.

Based on our numerical experiments, we conclude that significant amounts of energy can be generated by smart multi-well arrangements from hot sedimentary aquifers, potentially meeting the heat demand in densely populated cities as the city of Munich to a large extent. However, a detailed quantitative analysis is required for a sustainable and optimized reservoir development. Simulation results suggest that the complex thermo-hydraulic interaction between multiple wells and the heterogeneity of the reservoir rock permeability drive the optimal deployment of geothermal multi-well arrangements for the envisaged economic utilization time. Moreover, our computer experiments indicate that the combination of the developed numerical framework and multiple doublet arrays in a lattice structure is appropriate, on the one hand, for a comprehensive assessment of the extractable geothermal energy from deep geothermal reservoirs at a regional scale and, on the other hand, for the analysis of the impact of possible thermo-hydraulic interferences over a wide range of reservoir conditions and multi-well arrangements on the optimal net energy. Particularly, numerical simulations concerning multi-well hexagonal constellations placed around a fault damage zone reveal relevant thermo-hydraulic interactions in the optimal deployment, minimizing pressure difference between injectors and producers and maximizing thermal breakthrough occurrence time.

Our results show that an optimal positioning in heterogeneous reservoirs has a significant impact on the resulting net energy. Among the control variables, the distance between the wells has influenced the objective function (the net energy) the most.

The optimization processes evidence that within the imposed geometrical constraints, increasing the inter-well distance yields, on the one hand a delayed thermal breakthrough time. On the other hand, it might allow to deploy multiple wells in more favorable permeability structures. In addition, the case of linearly varying reservoir temperature field could not be identified as significantly influencing the positioning of wells in the considered geological and geophysical settings.

From our simulations, we further conclude that the developed computational framework is especially suitable for the investigation of long-term geothermal reservoir performance affected by a large numbers of multi-well arrangements with placement optimization purposes.

The implemented numerical method specifically facilitates the automatic search for the optimal deployment of smart multi-well arrangements, since it does not require to generate a new computational mesh when modifying the position of the wells. Modeling and simulation of coupled thermo-hydraulic reservoir processes resulting from the operation of diverse geothermal multi-well systems in numerous scenarios would otherwise be exceedingly time-consuming. Consequently, the methodology developed in this work may constitute an important tool in the large-scale development of hot sedimentary aquifers for district heating in urban regions worldwide.

Acknowledgments

This work has been partially supported by a Seed Grant of the Leibniz Mathematical Modeling and Simulation (MMS) Network.

References

[1] Susan M. Agar and Sebastian Geiger. Fundamental controls on fluid flow in carbonates: current workflows to emerging technologies. *Geological Society, London, Special Publications*, 406(1):1–59, 2015.

[2] Susan M. Agar and Gary J. Hampson. Fundamental controls on flow in carbonates: an introduction. *Petroleum Geoscience*, 20(1):3–5, 2014.

[3] Thorsten Agemar, Jessica-Aileen Alten, Britta Ganz, Jörg Kuder, Klaus Kühne, Sandra Schumacher, and Rüdiger Schulz. The Geothermal Information System for Germany - GeotIS. *Zeitschrift der Deutschen Gesellschaft für Geowissenschaften*, 165(2):129–144, 06 2014.

[4] Thorsten Agemar, Rüdiger Schellschmidt, and Rüdiger Schulz. Subsurface temperature distribution in Germany. *Geothermics*, 44:65 – 77, 2012.

[5] Thorsten Agemar, Josef Weber, and Rüdiger Schulz. Deep Geothermal Energy Production in Germany. *Energies*, 7(7):4397–4416, 2014.

[6] James Ahrens, Berk Geveci, and Charles Law. ParaView: An End-User Tool for Large Data Visualization. *Visualization Handbook*, 2005.

[7] M. S. Alnæs, J. Blechta, J. Hake, A. Johansson, B. Kehlet, A. Logg, C. Richardson, J. Ring, M. E. Rognes, and G. N. Wells. The FEniCS Project Version 1.5. *Archive of Numerical Software*, 3(100), 2015.

[8] Jessica-Aileen Alten, A. Thorsten, J. Gramenz, and M. Tribbensee, K. Wolf. GeotIS: Free Access to Maps and 3D Models for Geothermal Project Planning in Germany. In *Proceedings of the European Geothermal Congress*, 2019.

[9] Miklos Antics, R. Bertani, and B. Sanner. Summary of EGC 2016 Country Update Reports on Geothermal Energy in Europe. In *Proceedings of the European Geothermal Congress*, 2016.

[10] Miklos Antics and B. Sanner. Status of Geothermal Energy Use and Resources in Europe. In *Proceedings of the European Geothermal Congress*, 2007.

[11] D. Arndt, W. Bangerth, T. C. Clevenger, D. Davydov, M. Fehling, D. Garcia-Sanchez, G. Harper, T. Heister, L. Heltai, M. Kronbichler, R. M. Kynch, M. Maier, J.-P. Pelteret, B. Turcksin, and D. Wells. The `deal.II` Library, Version 9.1. *Journal of Numerical Mathematics*, 2019. accepted.

[12] G. R. Beardsmore and J. P. Cull. *Crustal Heat Flow: A Guide to Measurement and Modelling*. Cambridge University Press, 2001.

[13] R. Bertani, P. Dumas, J. Bonafin, O. G. Flóvenz, B. Jónsdóttir, A. Manzella, A. Donato, G. Gola, A. Santilano, E. Trumpy, S. Simsek, J.-D. van Wees, M. Pluymaekers, H. Veldkamp, S. van Gessel, D. Bonté, L. Rybach, B. Sanner, and L. Angelino. *Perspectives for Geothermal Energy in Europe*. World Scientific Publishing Europe Ltd., New York, 2017.

[14] Daniel Beyer, Cindy Kunkel, Michaela Aehnelt, Dieter Pudlo, Thomas Voigt, Georg Nover, and Reinhard Gaupp. Influence of depositional environment and diagenesis on petrophysical properties of clastic sediments (Buntsandstein of the Thuringian Syncline, Central Germany). *Zeitschrift der Deutschen Gesellschaft für Geowissenschaften*, 165(3):345–365, 2014.

[15] Lars Bilke, Bernd Flemisch, Thomas Kalbacher, Olaf Kolditz, Helmig Rainer, and Thomas Nagel. Development of Open-Source Porous Media Simulators: Principles and Experiences. *Transport in Porous Media*, 130(1):337–361, 2019.

[16] Johannes Birner. *Hydrogeologisches Modell des Malmaquifers im Süddeutschen Molassebecken - Hydrogeological model of the Malm aquifer in the South German Molasse Basin*. PhD thesis, Freie Universität Berlin, 2013.

[17] Laura Blank, Alfonso Caiazzo, Franz Chouly, Alexei Lozinski, and Joaquin Mura. Analysis of a stabilized penalty-free Nitsche method for the Brinkman, Stokes, and Darcy problems. *ESAIM: Mathematical Modeling and Numerical Analysis (M2AN)*, 52(6):2149–2185, 2018.

[18] M. Blatt, A. Burchardt, A. Dedner, Ch. Engwer, J. Fahlke, B. Flemisch, Ch. Gersbacher, C. Gräser, F. Gruber, Ch. Grüninger, D. Kempf, R. Klöfkorn, T. Malkmus, S. Müthing, M. Nolte, M. Piatkowski, and O. Sander. The Distributed and Unified Numerics Environment, Version 2.4. *Archive of Numerical Software*, 4(100):13–29, 2016.

[19] M. G. Blöcher, G. Zimmermann, I. Moeck, W. Brandt, A. Hassanzadegan, and F. Magri. 3D numerical modeling of hydrothermal processes during the lifetime of a deep geothermal reservoir. *Geofluids*, 10(3):406–421, 2010.

[20] Gudmundur S. Bödvarsson and Chin Fu Tsang. Injection and Thermal Breakthrough in Fractured Geothermal Reservoirs. *Journal of Geophysical Research: Solid Earth*, 87(B2):1031–1048, 1982.

[21] Christian Boissavy, P. Rocher, P. Laplaige, and C. Brange. Geothermal Energy Use, Country Update for France. In *Proceedings of the European Geothermal Congress*, 2016.

[22] H. C. Brinkman. A calculation of the viscous force exerted by a flowing fluid on a dense swarm of particles. *Applied Scientific Research*, 1(1):27–34, 1949.

[23] Geert K. Brouwer, A. Lokhorst, and B. Orlic. Geothermal Heat and Abandoned Gas Reservoirs in the Netherlands. In *Proceedings of the World Geothermal Congress*, 2005.

[24] H. Buness, H. Von Hartmann, E. Lüschen, E. Meneses Rioseco, B. Wawerzinek, J. Ziesch, and R. Thomas. GeoParaMol: Eine Integration verschiedener Methoden zur Reduzierung des Fündigkeitsrisikos in der bayrischen Molasse. *Geothermische Energie*, 85:22–23, 02 2016.

[25] M. Cacace, M. Scheck-Wenderoth, V. Noack, Y. Cherubini, and R. Schellschmidt. Modelling the Surface Heat Flow Distribution in the Area of Brandenburg (Northern Germany). *Energy Procedia*, 40:545 – 553, 2013.

[26] M. C. Cacas and J. M. Daniel. Nested geological modelling of naturally fractured reservoirs. *Petroleum Geoscience*, 7(5):43–52, 03 2001.

[27] L. Cattaneo and P. Zunino. A computational model of drug delivery through microcirculation to compare different tumor treatments. *International Journal for Numerical Methods in Biomedical Engineering*, 30(11):1347–1371, 2014.

[28] V. Cermak, H.G. Huckenholz, L. Rybach, R. Schmid, J.R. Schopper, M. Schuch, D. Stöfler, and J. Wohlenberg. Physical properties of rocks. In *Angenheister, G. (Ed.), vol. 1a*. Springer, Heidelberg, 1982.

[29] Philippe G. Ciarlet. *The finite element method for elliptic problems*, volume 40 of *Classics in Applied Mathematics*. Society for Industrial and Applied Mathematics (SIAM), Philadelphia, PA, 2002.

[30] C. Clauser, A. Koch, A. Hartmann, R. Jorand, V. Rath, A. Wolf, D. Mottaghy, and R. Pechnig. Erstellung statistisch abgesicherter termischer hydraulischer Gesteinseigenschaften für den flachen und tiefen Untergrund in Deutschland. Phase 1 - Westliche Molasse und nördlich angrenzendes Süddeutsches Schichtstufenland. Technical report, RWTH Aachen, 2006.

[31] Christoph Clauser and Ernst Huenges. *Thermal Conductivity of Rocks and Minerals*, pages 105–126. American Geophysical Union (AGU), 2013.

[32] R.A. Crooijmans, C.J.L. Willems, H.M. Nick, and D.F. Bruhn. The influence of facies heterogeneity on the doublet performance in low-enthalpy geothermal sedimentary reservoirs. *Geothermics*, 64:209–219, nov 2016.

[33] C. D'Angelo. Finite Element Approximation of Elliptic Problems with Dirac Measure Terms in Weighted Spaces: Applications to One- and Three-dimensional Coupled Problems. *SIAM J. Numer. Anal.*, 50(1):194–215, 2012.

[34] Frank Dethlefsen, Markus Ebert, and Andreas Dahmke. A geological database for parameterization in numerical modeling of subsurface storage in northern Germany. *Environmental Earth Sciences*, 71(5):2227–2244, Mar 2014.

[35] H.-J. G. Diersch. *FEFLOW. Finite Element Modeling of Flow, Mass and Heat Transport in Porous and Fractured Media*. Springer Science + Business Media; Springer Heidelberg Dordrecht London, 2014.

[36] Mohammad A. Al Dossary and Hadi Nasrabadi. Well placement optimization using imperialist competitive algorithm. *Journal of Petroleum Science and Engineering*, 147:237 – 248, 2016.

[37] M. Dussel, E. Lüschen, R. Thomas, T. Agemar, T. Fritzer, S. Sieblitz, B. Huber, J. Birner, and R. Schulz. Forecast for thermal water use from Upper Jurassic carbonates in the Munich region (South German Molasse Basin). *Geothermics*, 60:13 – 30, 2016.

[38] Michael Dussel, I. Moeck, M. Wolfgramm, and R. Straubinger. Characterization of a Deep Fault Zone in Upper Jurassic Carbonates of the Northern Alpine Foreland Basin for Geotherma Production (South Germany). In *Proceedings of the 43rd Workshop on Geothermal Reservoir Engineering*, 2018.

[39] Alexandre Ern and Jean-Luc Guermond. *Theory and practice of finite elements*, volume 159 of *Applied Mathematical Sciences*. Springer-Verlag, New York, 2004.

[40] H. Ernst, editor. *Geothermal Energy Systems: Exploration, Development, and Utilization*. WILEY-VCH Verlag GmbH & Co. KGaA, Weinheim, 2010.

[41] Andrea Förster. Analysis of borehole temperature data in the Northeast German Basin: continuous logs versus bottom-hole temperatures. *Petroleum Geoscience*, 7:241–254, 2001.

[42] Andrea Förster and Daniel F. Merriam. *Geothermics in Basin Analysis*. Computer Applications in the Earth Sciences. Springer US; Kluwer Academic/Plenum Publishers, 1999.

[43] H. Frisch and B. Huber. Versuch einer Bilanzierung des Thermalwasservorkommens im Malmkarst des süddeutschen Molassebeckens. *Hydrogeologie und Umwelt*, 20:25–43, 12 2000.

[44] T. Fritzer. Bayerischer Geothermieatlas - Hydrothermale Energiegewinnung: Technik, wirtschaftliche Aspekte, Risiken, hydrothermale Grundwasserleiter in Bayern, Untergrundtemperaturen in Bayern. Technical report, Bayerisches Staatsministerium für Wirtschaft, Infrastruktur, Verkehr und Technologie, Munich, 2010.

[45] Sven Fuchs. The variability of rock thermal properties in sedimentary basins and the impact on temperature modelling – a Danish example. *Geothermics*, 76:1 – 14, 2018.

[46] Sven Fuchs and Andrea Förster. Rock thermal conductivity of Mesozoic geothermal aquifers in the Northeast German Basin. *Chemie der Erde – Geochemistry*, 70:13 – 22, 2010.

[47] J. M. Gablonsky and C. T. Kelley. A locally-biased form of the DIRECT algorithm. *J. Global Optim.*, 21(1):27–37, 2001.

[48] S. Ganesan, V. John, G. Matthies, R. Meesala, A. Shamim, and U. Wilbrandt. An Object Oriented Parallel Finite Element Scheme for Computations of PDEs: Design and Implementation. In *2016 IEEE 23rd International Conference on High Performance Computing Workshops (HiPCW)*, pages 106–115, Dec 2016.

[49] Christophe Geuzaine and Jean-FranÃğois Remacle. Gmsh: A 3-d finite element mesh generator with built-in pre- and post-processing facilities. *International Journal for Numerical Methods in Engineering*, 79(11):1309–1331, 2009.

[50] Reza Ghasemizadeh, Xue Yu, Christoph Butscher, Ferdi Hellweger, Ingrid Padilla, and Akram Alshawabkeh. Equivalent Porous Media (EPM) Simulation of Groundwater Hydraulics and Contaminant Transport in Karst Aquifers. *PLOS ONE*, 10(9):1–21, 2015.

[51] Ed.: Ralph Haenel, editor. *The Urach geothermal project (Swabian Alb, Germany)*. Schweizerbart Science Publishers, Stuttgart, Germany, 03 1982.

[52] R. Haenel, M. Kleefeld, and I. Koppe. Geothermisches Energiepotential, Pilotstudie: Abschätzung der geothermischen Energievorräte an ausgewählten Beispielen in der Bundesrepublik Deutschland. Technical report, Final report (Abschlussberricht), Bericht NLfB, Archive Nr. 96276, Bd. I-IV. Niedersächsisches Landesamt für Bodenforschung, Hannover, Germany, 1984.

[53] R. Haenel, L Rybach, and L. Stegena, editors. *Fundamentals of Geothermics*, pages 9–57. Springer Netherlands, 1988.

[54] R. Haenel and E. Staroste. Atlas of Geothermal Resources in the European Community, Austria and Switzerland. Technical report, Niedersächsisches Landesamt für Bodenforschung, Hannover, Germany, 1988.

[55] R. Haenel, L. Stegena, and L. Rybach. *Handbook of Terrestrial Heat-Flow Density Determination: with Guidelines and Recommendations of the International Heat Flow Commission*. Springer Netherlands, 2012.

[56] C. Hecht and C. Pletl. Das Verbundprojekt GRAME - Wegweiser für eine geothermische Wärmeversorgung urbaner Ballungsräume. *Geothermische Energie*, 82(2), 02 2015.

[57] S. Hurter and R. Haenel. Atlas of Geothermal Resources in Europe: Planning Exploration and Investments. In *Proceedings of the World Geothermal Congress*, 2000.

[58] Suzanne Hurter and RÃijdiger Schellschmidt. Atlas of geothermal resources in Europe. *Geothermics*, 32(4):779 – 787, 2003.

[59] M. Jobmann and R. Schulz. Hydrogeothermische Energiebilanz und Grundwasserhaushalt des Malmkarstes im süddeutschen Molassebecken. Technical Report Archive Nr. 105040, Niedersächsisches Landesamt für Bodenforschung, 1989.

[60] S. G. Johnson. The nlopt nonlinear-optimization package. http://github.com/stevengj/nlopt.

[61] Ali Joodi, Stanislas Sizaret, StÃľphane Binet, Bruand A., Patrick AlbÃľric, and Michel Lepiller. Development of a Darcy-Brinkman model to simulate water flow and tracer transport in a heterogeneous karstic aquifer (Val d'Orléans, France). *Hydrogeology Journal*, 18:295–309, 03 2009.

[62] S. Kahrobaei, R.M. Fonseca, C.J.L. Willems, F. Wilschut, and J.D. van Wees. Regional scale geothermal field development optimization under geological uncertainties. In *Proceedings of the European Geothermal Congress*, 2019.

[63] A. Koch, R. Jorand, C. Vogt, J.-C. Arnold, D. Mottaghy, R. Pechnig, and C. Clauser. Erstellung statistisch abgesicherter termischer hydraulischer Gesteinseigenschaften für den flachen und tiefen Untergrund in Deutschland. Phase 2 - Westliches Nordrhein-Westfalen und bayerisches Molassebecken. Technical report, RWTH Aachen, 2009.

[64] Jörg Kuder, Franz Binot, Wiete Hübner, Judith Orilski, Thomas Wonik, and Rüdiger Schulz. Für die Geothermie wichtige hydraulische Parameter von Gesteinen des Valangin und der Bückeberg-Formation (Wealden) in Nordwestdeutschland. *Zeitschrift der Deutschen Gesellschaft für Geowissenschaften*, 165(3):455–467, 08 2014.

[65] Ilmo T. Kukkonen and Argo JÃţeleht. Weichselian temperatures from geothermal heat flow data. *Journal of Geophysical Research: Solid Earth*, 108(B3), 2003.

[66] Cindy Kunkel, Michaela Aehnelt, Dieter Pudlo, Nina Kukowski, Kai Uwe Totsche, and Reinhard Gaupp. Subsurface aquifer heterogeneities of Lower Triassic clastic sediments in central Germany. *Marine and Petroleum Geology*, 97:209 – 222, 2018.

[67] Małgorzata Labus and Krzysztof Labus. Thermal conductivity and diffusivity of fine-grained sedimentary rocks. *Journal of Thermal Analysis and Calorimetry*, 132(3):1669–1676, Jun 2018.

[68] Tianyu Li, Sogo Shiozawa, and Mark W. McClure. Thermal breakthrough calculations to optimize design of a multiple-stage Enhanced Geothermal System. *Geothermics*, 64:455 – 465, 2016.

[69] Jon Limberger, Thijs Boxem, Maarten Pluymaekers, David Bruhn, Adele Manzella, Philippe Calcagno, Fred Beekman, Sierd Cloetingh, and Jan-Diederik van Wees. Geothermal energy in deep aquifers: A global assessment of the resource base for direct heat utilization. *Renewable and Sustainable Energy Reviews*, 82:961 – 975, 2018.

[70] D. Liu and J. Sun. *The Control Theory and Application for Well Pattern Optimization of Heterogeneous Sandstone Reservoirs*. Petroleum Industry Press and Springer-Verlag, Berlin Heidelberg, 2017.

[71] E. M. Llanos, S. J. Zarrouk, and R. A. Hogarth. Simulation of the Habanero Enhanced Geothermal System (EGS), Australia. In *Proceedings of the World Geothermal Congress*, 2015.

[72] John W. Lund and Tonya L. Boyd. Direct utilization of geothermal energy 2015 worldwide review. *Geothermics*, 60:66 – 93, 2016.

[73] Ewald Lüschen, Markus Wolfgramm, Thomas Fritzer, Michael Dussel, Rüdiger Thomas, and Rüdiger Schulz. 3D seismic survey explores geothermal targets for reservoir characterization at Unterhaching, Munich, Germany. *Geothermics*, 50:167 – 179, 2014.

[74] Jacek Majorowicz and Stanislaw Wybraniec. New terrestrial heat flow map of Europe after regional paleoclimatic correction application. *International Journal of Earth Sciences*, 100(4):881–887, Jun 2011.

[75] Michael G. McDonald and Arlen W. Harbaugh. The history of MODFLOW. *Ground Water*, 2005.

[76] Ernesto Meneses Rioseco, J. Ziesch, H. Von Hartmann, and H. Buness. Geothermal reservoir modelling and simulation of the Upper Jurassic aquifer for district heating in the city of Munich (Germany). In *Proceedings of the European Geothermal Congress*, 2019.

[77] Ernesto Meneses Rioseco, J. Ziesch, B. Wawerzinek, H. Von Hartmann, R. Thomas, and H. Buness. 3-d Geothermal Reservoir Modeling of the Upper Jurassic Carbonate Aquifer in the City of Munich (Germany) under the Thermal-Hydraulic Influence of Optimized Geothermal Multi-Well Patterns - Project GeoParaMol. In *Proceedings of the 43rd Workshop on Geothermal Reservoir Engineering*, 2018.

[78] Inga S. Moeck. Catalog of geothermal play types based on geologic controls. *Renewable and Sustainable Energy Reviews*, 37:867 – 882, 2014.

[79] E. Mraz, M. Wolfgramm, I. Moeck, and K. Thuro. Detailed Fluid Inclusion and Stable Isotope Analysis on Deep Carbonates from the North Alpine Foreland Basin to Constrain Paleofluid Evolution. *Geofluids*, 2019:23 pages, 2019.

[80] Vera Noack, Yvonne Cherubini, Magdalena Scheck-Wenderoth, BjÃűrn Lewerenz, Thomas Höding, Andreas Simon, and Inga Moeck. Assessment of the present-day thermal field (NE German Basin) – Inferences from 3D modelling. *Chemie der Erde – Geochemistry*, 70:47 – 62, 2010.

[81] Mette Olivarius, Rikke Weibel, Morten L. Hjuler, Lars Kristensen, Anders Mathiesen, Lars H. Nielsen, and Claus Kjøller. Diagenetic effects on porosity-permeability relationships in red beds of the Lower Triassic Bunter Sandstone Formation in the North German Basin. *Sedimentary Geology*, 321:139 – 153, 2015.

[82] Adrián E. Ortiz Rojas, Michael Dussel, and Inga Moeck. Borehole geophysical characterisation of a major fault zone in the geothermal Unterhaching gt 2 well, South German Molasse Basin. *Zeitschrift der Deutschen Gesellschaft für Geowissenschaften*, 169(3):445–463, 10 2018.

[83] M. J. O'Sullivan. Geothermal reservoir simulation. *International Journal of Energy Research*, 9(3):319–332, 1985.

[84] Michael J. O'Sullivan, Karsten Pruess, and Marcelo J. Lippmann. State of the art of geothermal reservoir simulation. *Geothermics*, 30(4):395 – 429, 2001.

[85] Han-Young Park, Changdong Yang, Ahmad D. Al-Aruri, and Paul A. Fjerstad. Improved decision making with new efficient workflows for well placement optimization. *Journal of Petroleum Science and Engineering*, 152:81 – 90, 2017.

[86] Charles S Peskin. The immersed boundary method. *Acta Numerica*, 11(1):479–517, jan 2002.

[87] M.P.D. Pluymaekers, L. Kramers, J.-D. van Wees, A. Kronimus, S. Nelskamp, T. Boxem, and D. Bonté. Reservoir characterisation of aquifers for direct heat production: Methodology and screening of the potential reservoirs for the Netherlands. *Netherlands Journal of Geosciences - Geologie En Mijnbouw*, 91(4):621âĂŞ636, 2012.

[88] Peter Popov, Yalchin Efendiev, and Guan Qin. Multiscale modeling and simulations of flows in naturally fractured Karst reservoirs. *Commun. Comput. Phys.*, 6(1):162–184, 2009.

[89] Luis Miguel Rios and Nikolaos V. Sahinidis. Derivative-free optimization: a review of algorithms and comparison of software implementations. *Journal of Global Optimization*, 56:1247–1293, 2013.

[90] Auref Rostamian, Saeid Jamshidi, and Emily Zirbes. The development of a novel multi-objective optimization framework for non-vertical well placement based on a modified non-dominated sorting genetic algorithm-ii. *Computational Geosciences*, Aug 2019.

[91] L. Rybach. Geothermal systems, conductive heat flow, geothermal anomalies. In *Geothermal Systems: Principles and case histories*, pages 3–31. John Wiley & Sons, 1981.

[92] Sanaz Saeid, Rafid Al-Khoury, Hamidreza H. Nick, and Michael A. Hicks. A prototype design model for deep low-enthalpy hydrothermal systems. *Renewable Energy*, 77:408–422, may 2015.

[93] Sanaz Saeid, Rafid Al-Khoury, Hamidreza H. M. Nick, and Frans Barends. ExperimentalâĂŞnumerical study of heat flow in deep low-enthalpy geothermal conditions. *Renewable Energy*, 62:716 – 730, 2014.

[94] Mohammad Sayyafzadeh. Reducing the computation time of well placement optimisation problems using self-adaptive metamodelling. *Journal of Petroleum Science and Engineering*, 151:143 – 158, 2017.

[95] A. E. Scheidegger. General theory of dispersion in porous media. *Journal of Geophysical Research (1896-1977)*, 66(10):3273–3278, 1961.

[96] Felina Schütz, Gerd Winterleitner, and Ernst Huenges. Geothermal exploration in a sedimentary basin: new continuous temperature data and physical rock properties from northern Oman. *Geothermal Energy*, 6(1):5, Mar 2018.

[97] Homuth Sebastian, A. E. Götz, and I. Sass. Reservoir characterization of the Upper Jurassic geothermal target formations (Molasse Basin, Germany): role of thermofacies as exploration tool. *Geothermal Energy Science*, 3:41–49, 2015.

[98] G.Michael Shook. Predicting thermal breakthrough in heterogeneous media from tracer tests. *Geothermics*, 30(6):573 – 589, 2001.

[99] I. Stober and K. Bucher. *Geothermal Energy. From Theoretical Models to Exploration and Development*. Springer-Verlag, Berlin Heidelberg, 2013.

[100] Ingrid Stober. *Strömungsverhalten in Festgesteinsaquiferen mit Hilfe von Pump- und Injektionsversuchen*. Schweizerbart Science Publishers, Stuttgart, Germany, 09 1986.

[101] Ingrid Stober, Marco Jodocy, and Benedikt Hintersberger. Comparison of hydraulic conductivities determined with different methods in the Upper Jurassic of the southwest German Molasse Basin. *Zeitschrift der Deutschen Gesellschaft für Geowissenschaften*, 164(4):663–679, 12 2013.

[102] Pierre Ungemach and M. Antics. Assessment of Deep Seated Geothermal Reservoirs in Selected European Sedimentary Environments. In *Proceedings of the World Geothermal Congress*, 2015.

[103] Robert Vörös, Ralph Weidler, Lambertus De Graaf, and Doone Wyborn. Thermal modelling of long term circulation of multi-well development at the Cooper Basin hot fractured rock (HFR) project and current proposed scale-up program. In *Proceedings of the 32nd Workshop on Geothermal Reservoir Engineering*, 2007.

[104] Josef Weber, H. Born, and I. Moeck. Geothermal Energy Use, Country Update for Germany 2016 - 2018. In *Proceedings of the European Geothermal Congress*, 2019.

[105] U. Wilbrandt, C. Bartsch, N. Ahmed, N. Alia, F. Anker, L. Blank, A. Caiazzo, S. Ganesan, S. Giere, G. Matthies, R. Meesala, A. Shamim, J. Venkatesan, and V. John. Parmoon – a modernized program package based on mapped finite elements. *Computers and Mathematics with Applications*, 2016.

[106] Cees J.L. Willems, Hamidreza M. Nick, Gert Jan Weltje, and David F. Bruhn. An evaluation of interferences in heat production from low enthalpy geothermal doublets systems. *Energy*, 135:500–512, 2017.

[107] C.J.L. Willems, T. Goense, Hamidreza M. Nick, and D.F. Bruhn. The Relation Between Well Spacing and Net Present Value in Fluvial Hot Sedimentary Aquifer Geothermal Doublets: a West Netherlands Basin Case Study. In *Proceedings of the 41st Workshop on Geothermal Resevoir Engineering*, 2016.

[108] C.J.L. Willems, H.M. Nick, T. Goense, and D.F. Bruhn. The impact of reduction of doublet well spacing on the Net Present Value and the life time of fluvial Hot Sedimentary Aquifer doublets. *Geothermics*, 68:54 – 66, 2017.

[109] Liming Zhang, Zekun Deng, Kai Zhang, Tao Long, Joshua Desbordes, Hai Sun, and Yongfei Yang. Well-Placement Optimization in an Enhanced Geothermal System Based on the Fracture Continuum Method and 0-1 Programming. *Energies*, 12:709, 02 2019.